

Density Studies on SSX

Tim Gray

tgray1@swarthmore.edu

Swarthmore College Department of Physics
500 College Avenue, Swarthmore, PA 19081



Density Studies on SSX

Tim Gray

tgray1@swarthmore.edu

Swarthmore College Department of Physics

500 College Avenue, Swarthmore, PA 19081

March 19, 2001

Abstract

Using a visible light HeNe interferometer, operating at 632.8 nm, we measure the line-averaged density of spheromaks in the SSX experiment. Phase shift ambiguities associated with normal interferometers are resolved by circularly polarizing the reference beam and sending the recombined output of the interferometer through a Wollaston prism, which generates two outputs 90° out of phase with each other. The plasma densities measured are correlated with triple probe measurements of density and electron temperature.

Contents

1	Introduction	1
2	Basic Spheromak Physics	3
2.1	Plasma Confinement	3
2.2	Spheromak Formation	4
3	Interferometry	6
3.1	Introduction to Interferometry	6
3.2	Wave Dispersion Relation and Phase Shift	7
3.3	Heterodyne Interferometry	10
4	Langmuir Probe	13
4.1	The Simple Langmuir Probe	13
4.2	The Triple Probe	14
5	Experimental Setup	16
5.1	Physical Dimensions	16
5.2	Operating Parameters	17
5.3	Interferometer Construction	20
5.4	Triple Probe Construction	22
6	Experimental Results	24
6.1	Interferometer Data	24
6.2	Triple Probe Data	26
7	Future Directions	29
 <i>Appendicies</i>		
A	Interferometer Setup	30
B	Component Specifications	33

C	Gas Density Calibration	36
D	Analysis Routines	40
	D.1 Interferometer Routine	40
	D.2 Triple Probe Routine	41
E	Acknowledgements	44
	References	45

List of Tables

1	SSX Plasma Parameters	20
2	Component List	35

List of Figures

1	Solar Flare	1
2	Magnetic Reconnection	2
3	Anatomy of a Spheromak	3
4	Frozen-in-flux	4
5	Spheromak formation	5
6	Wave interference	6
7	Mach-Zehnder interferometer	7
8	Heterodyne interferometry	10
9	Waveplates and Wollastons	11
10	Probe Characteristic	13
11	Triple Probe Circuit	15
12	Triple Probe Dependencies	16
13	Pictures of SSX	17
14	Experimental setup	18
15	Typical Gun Shot	19
16	Stuffing Flux	19
17	Mount design	21
18	Picture of Triple Probe	22
19	Typical Interferometer Data	24
20	Density vs. Gun Flux	25
21	Typical Triple Probe Data	26
22	Radial Profile of Temperature and Density	28
23	Radial Profile of Temperature and Density	28
24	Interferometer setup	31
25	Gas Density Calibration - Detector Output	37
26	Gas Density Calibration - Fringe Shift	37
27	Helium Gas Calibration - Detector Output	38
28	Helium Gas Calibration - Fringe Shift	38

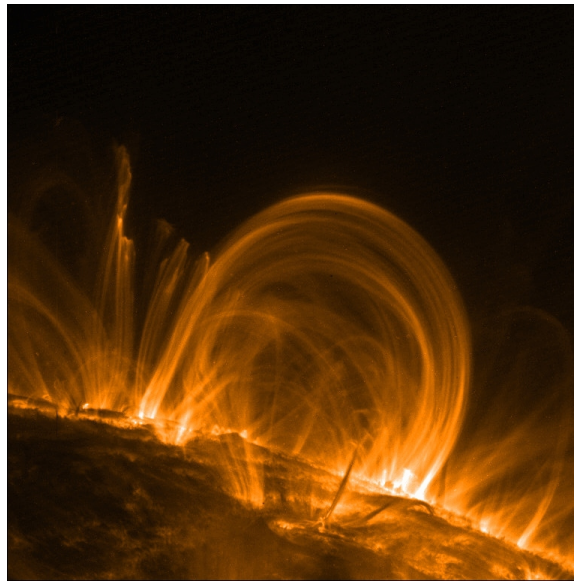


Figure 1: A solar flare as seen from the TRACE (Transition Region and Coronal Explorer) satellite. (NASA)

1 Introduction

Plasma is often described as the fourth state of matter. It can be thought of as a superheated gas, where the individual electrons acquire enough energy to ionize. This produces a mixture composed of electrons and ions. Since the plasma is presumably formed from some substance that is neutral before ionization, plasmas are often neutral or very close to neutral when taken as a whole. In fact, quasi-neutrality is part of the definition of plasma. However, since plasmas consist of unbound charges, they become good conductors.

Conductors can have the ability to possess high amounts of current flowing through them. Basic electromagnetic theory states that whenever you have charges, you have electric fields and whenever you have moving charges, i.e. current, you have magnetic fields. This means that plasmas are affected by magnetic and electric fields and often have magnetic fields.

Plasmas with embedded magnetic fields provide interesting magneto-fluid phenomenon. One such phenomena is magnetic reconnection. Magnetic reconnection occurs when two anti-parallel field lines merge and settle into a new equilibrium state, as shown in figure 2. Magnetic reconnection occurs naturally in many processes, the most prominent being in solar flares, as seen in figure 1. It is believed that magnetic reconnection governs the solar flare process, particularly in the releasing of energy.

The Swarthmore Spheromak Experiment (SSX) studies magnetic reconnection in the form of two merging toroidal plasmas, called spheromaks, with self confining toroidal and poloidal fields (figure 3). There is no need for apparatus in the ‘hole’ of the spheromak, enabling it to translate in an appropriate container, so it is ideally suited for formation at a site different from the measurement site. In SSX, this characteristic enables us to generate

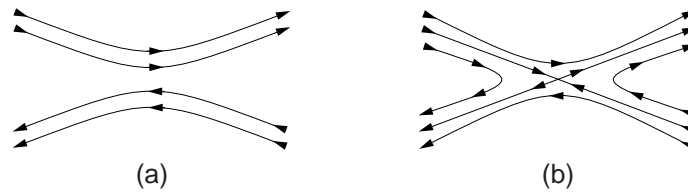


Figure 2: Magnetic Reconnection. (a) Two field lines of opposing direction come and merge, causing (b) some of the field to annihilate and reconnect on the sides. The annihilation of field lines converts the energy stored in the \mathbf{B} field in the form of the kinetic energy. This increase of kinetic energy accelerates the plasma out of the reconnection region.

two spheromaks at a formation site and send them to a separate interaction site free of the interference and fields of the formation equipment. These two spheromaks can then interact via the process of magnetic reconnection.

Since plasmas do have magnetic fields, it is relatively easy (in theory) to measure the electromagnetic properties of plasmas. “Tangible” characteristics such as density are often harder to measure. One way to measure the density of a plasma is to use interferometric techniques.

Interferometry has been around for a long time. One of the most famous of interferometers to be used in the name of science was the instrument designed by Albert Michelson and Edward Morley to measure the motion that the æther induces in light waves. Their device was so accurate that they discovered that the æther did not induce a change in the speed of light, leading to the conclusion that the æther did not exist, thus laying the groundwork for Albert Einstein’s Theory of Special Relativity.

Interferometry relies on the interference between two or more beams of light. Changes in the density of the plasma create predictable phase shifts in the light transversing it. This allows for a non-intrusive method for measuring plasma density.

Another more common method of measuring the density and the temperature is to use a Langmuir probe, which consists of a conductor situated in the plasma. Though very simple in construction, relatively detailed measurements can be obtained. Unfortunately, Langmuir probes are intrusive and can disrupt the physics of the experiment.

This thesis explores some of the general characteristics of spheromaks, methods for extracting specific characteristics, and a set of findings based on these two methods.

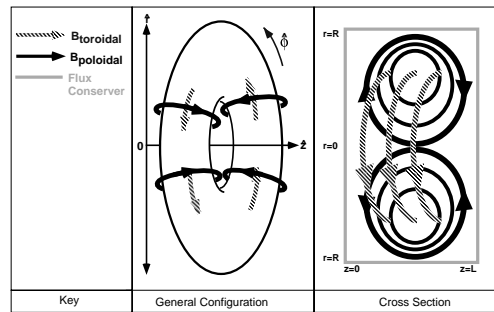


Figure 3: A spheromak consists of a toroidal ‘donut’ of plasma with self confining toroidal and poloidal fields. Spheromaks in SSX are confined by means of a flux conserver.

2 Basic Spheromak Physics

2.1 Plasma Confinement

As previously mentioned, plasma is an ionized gas. The energies often needed to ionize a gas are on the order of magnitude of a few eV^1 , so the particles in a typical plasma are quite “hot.” With particles this energetic, it is relatively easy for them to reach the edge of the container holding them and recombine at the wall. Thus, confinement schemes are needed in order to create a plasma which will remain without regenerating it. Since a plasma is composed of electrons and ions, one can develop magnetic confinement schemes, using the fact that charged particles will feel a force $\mathbf{F} = q\mathbf{v} \times \mathbf{B}$ while moving in magnetic field.

One can construct a complicated confinement mechanism for plasmas, but the spheromak is confined by one of the simplest ones. By imbuing the spheromak with poloidal and toroidal currents (figure 3), which generate the toroidal and poloidal magnetic fields, the spheromak provides for its own confinement as long as the toroidal field of the spheromak is zero at the wall of the vessel containing it. Most other types of magnetic confinement do not have this condition; as a result, large external magnets are often used to generate the necessary fields. In the case of tokamaks and stellarators in particular, one must put confinement apparatus in the ‘hole’ of the torus, robbing the plasma of any large scale mobility.

All that is needed to ensure that the toroidal magnetic field is zero at the vessel wall is the use of a “flux conserver”. A flux conserver is simply a container made out of conductive copper. Being a conductor, the copper does not allow for flux to pass through it very quickly. Whenever a current approaches the flux conserver wall, an image current flows in the copper, preventing the magnetic field from passing through. Since the plasma obeys something called the frozen-in-flux constraint and flux is not allowed to pass through the flux conserver, the plasma is contained. The frozen-in-flux constraint basically states that all the magnetic field lines in the plasma are frozen into the plasma itself; when the plasma moves, the particular field lines associated with it also move, as shown in figure 4 (Kornack, 1998). This feature arises from the plasma being a perfect conductor. Any electric fields are

¹1 eV = 11,604 K

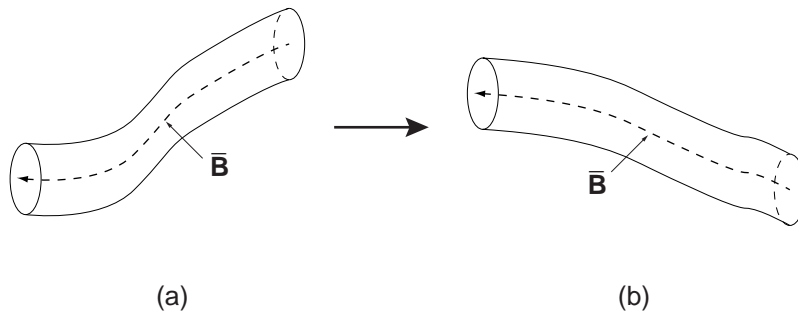


Figure 4: As a tube of plasma moves from configuration (a) to configuration (b), the magnetic field line this “flux tube” encircles moves with it.

immediately cancelled by moving charges in the plasma, and any change in the magnetic flux is likewise prevented. As a result, the plasma can only move along contours of constant flux, preventing it from moving with respect to the magnetic fields. The magnetic fields and plasma form a magnetofluid. Any external fields applied to this magnetofluid affect it as a whole; the component magnetic fields and plasma cannot act independently. Thus, the currents that are driven in the plasma itself are enough to provide for confinement.

Since spheromaks are elegantly self-sufficient with respect to confinement, one is able to utilize them in ways that many other plasmas cannot be used. The most obvious is the generation of a spheromak at a place remote from an interaction site where measurements are done. This allows for the use of instrumentation that would normally be of no use due to the inherent noise of the generation processes.

2.2 Spheromak Formation

Spheromaks are formed in SSX by means of magnetic coaxial guns. Gas is puffed into guns by means of specially designed valves (see figure 14 on page 18) (Kornack, 1998). Once the gas is introduced into the gap between the inner and outer electrodes of the gun (figure 5a), a capacitor bank discharges approximately 5 kV across the electrodes, ionizing the gas in the gap (figure 5b). Current flowing through the plasma and electrodes interacts with its magnetic field, accelerating the plasma out of the gun. A stuffing field is applied to the center electrode of the gun. When the plasma encounters this field at the opening of the gun and resists the change in field according to Faraday’s law, currents flow in the plasma as the stuffing field distends (figure 5c). Given enough magnetic pressure, the torus of plasma can exceed the tension of the stuffing field, breaking away to form a spheromak (figure 5d). This can be likened to blowing soap bubbles. The plasma encountering this stuffing field is similar to one blowing on the soap film; given the right conditions, the soap film distends and reconnects with itself, forming an independent bubble.

The spheromak is not stable once it is generated. As stated in section 2.1, the plasma behaves according to the frozen-in-flux constraint. If there is nothing to contain the magnetic fields, then nothing will contain the plasma and the spheromak will just dissipate. The flux conserver confines the magnetic fields, which then holds back the plasma. However, as

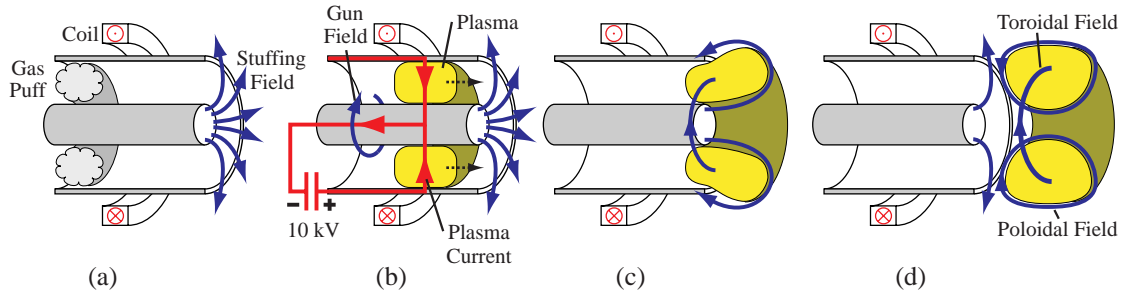


Figure 5: Spheromak formation in a magnetic coaxial gun. (a) Gas is puffed into the gun and a magnetic stuffing field is applied to the inner electrode by the electromagnetic coils. (b) A large potential is applied to the inner and outer electrodes, which leads to the creation of plasma and the toroidal gun field. (c) The toroidal plasma moves further down the “gun barrel” and the stuffing field wraps around the plasma. (d) The stuffing field pinches off around the plasma, creating the poloidal field of the plasma, while the gun field creates the toroidal field of the plasma. A spheromak is born.

the spheromak exits the gun, it does have room to expand somewhat into the larger flux conserver. The spheromak relaxes into an equilibrium state of the lowest energy configuration of the magnetic fields with the pressure forces of the plasma (Kornack, 1998). This equilibrium is described most simply by balancing the particle forces in the plasma with the magnetic (Lorentz) forces, as shown in the following equation:

$$\begin{aligned} \rho \frac{\partial \mathbf{v}}{\partial t} &= -\nabla p + \mathbf{J} \times \mathbf{B} = 0 \\ \nabla p &= \mathbf{J} \times \mathbf{B} \end{aligned} \quad (1)$$

Spheromaks are defined as low β plasmas, where β is defined in equation 2.

$$\beta \equiv \frac{\Sigma nkT}{\frac{B^2}{2\mu_0}} = \frac{\text{Particle pressure}}{\text{Magnetic field pressure}} \quad (2)$$

Because of this, one can assume that $\nabla p \rightarrow 0$. This simply means that only the $\mathbf{J} \times \mathbf{B}$ contributes to the equilibrium of the plasma. Thus, equation 1 can be rewritten as:

$$\mathbf{J} \times \mathbf{B} = 0 \quad (3)$$

Since we know from Ampere’s Law that $\mathbf{J} \propto \nabla \times \mathbf{B}$, this equation can be written as:

$$\nabla \times \mathbf{B} \times \mathbf{B} = 0 \quad (4)$$

Since $\nabla \times \mathbf{B} \parallel \mathbf{B}$,

$$\nabla \times \mathbf{B} = \lambda \mathbf{B} \quad (5)$$

where λ can either be a constant or a function of flux. Solutions of constant λ (from equation 5) for circular boundary conditions are a decent approximation to the first order for spheromaks in SSX (Geddes, 1997).

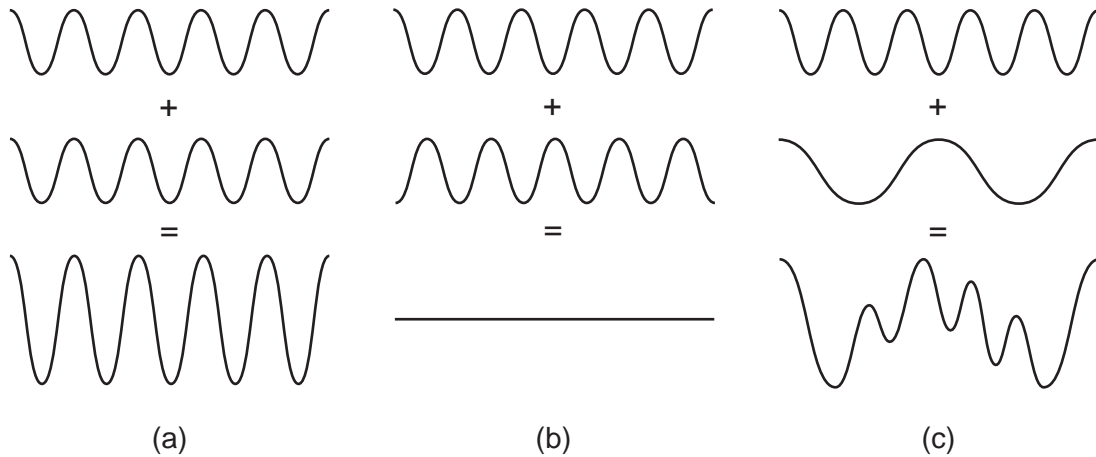


Figure 6: Examples of interference: (a) constructive interference (b) destructive interference (c) a combination of the two.

3 Interferometry

3.1 Introduction to Interferometry

Basic interferometry uses the wave nature of light to make extremely precise measurements. Interferometry has been around since the beginning of the 1800's, when Thomas Young laid the foundations for it with his double-slit interference experiment. The basic principle behind interferometry is sending a source of light down two or more paths and recombining them at some later point. Due to small differences in the optical paths of the separated beams, when the beams are recombined at a detector, interference patterns form.

Interference patterns occur when two sources of light recombine. Depending on the phase differences of the light sources, the light waves can either add constructively (peak plus peak) leading to bright areas or destructively (peak plus trough), which results in dark fringes (figure 6). Since the difference between a light and a dark fringe is only one half of a wavelength of light, one is able to measure path length differences with extreme precision.

Since interferometry is so heavily dependent on wavelength, it is often necessary to find light sources that are easily filtered or put out a very narrow range of wavelengths. With the invention of the laser, this has become a moot point. The single wavelength output of lasers make them very easy to use in the creation of interference patterns. As an added bonus, lasers are coherent light sources, allowing them to pass over long distances with little divergence. This breakthrough in technology has allowed interferometry to progress tremendously.

In this setup, we used a Mach-Zehnder interferometer, as shown in figure 7. The advantages of the Mach-Zehnder interferometer are that one can get a large separation between the reference beam and the scene beam and that each beam only traverses its path once, unlike other types of interferometers, such as a Michelson interferometer.

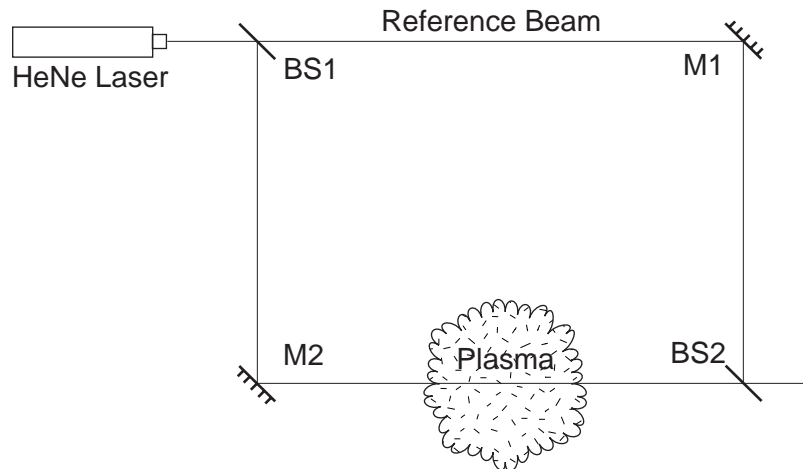


Figure 7: A basic Mach-Zehnder interferometer.

Traditionally, interferometers were used to measure many things, such as spherical aberration in lenses or air flow around objects. However, due to the electromagnetic properties of plasma, one is able to use interferometry to measure the average density of plasma over a straight line. In order to make this measurement, one must use a source of light which possesses a frequency higher than the frequency of the plasma (ω_{pe}). In plasmas, the electrons are much more mobile than the ions due to the electrons' lighter mass. Since they possess this mobility, they try to establish neutrality in the plasma. Because of their inertia, the electrons tend to overshoot the ions, oscillating around them. This frequency of oscillation is the plasma frequency ω_{pe} . A simple Helium Neon laser (HeNe), with a frequency of 4.741×10^{14} Hz, is sufficient in most plasmas.

As one tunes the interferometer into better alignment, the size of the fringes present grows, until finally, the output of the interferometer is either all dark or all light, since one has focused down to an individual trough or peak. Where one focuses the interferometer depends on the application. It is easy to set a detector on a fringe in a many fringe pattern by spreading the output of the interferometer with some type of objective lens. However, this “throws away” a lot of the output. When measuring extremely dynamic plasmas like a spheromak, with lifetimes in the microseconds, it is necessary to use extremely fast detectors. Often, detector signal strength is sacrificed for speed. As a result, “throwing away” interferometer output is a bad idea when using fast detectors. Thus, in this case, we closely aligned the interferometer and chose not to spread the output with objectives, allowing us to utilize the most of the output of our HeNe laser and enabling our use of fast detectors.

3.2 Wave Dispersion Relation and Phase Shift

When the interferometer is set up properly, the presence of plasma will introduce a phase shift in the scene beam, causing fringes to shift in the output. This phase shift is calculated

by first calculating the wave dispersion relation for plasma, starting from Faraday's law (eq. 6) and Ampere's law (eq. 7).

$$\nabla \times \mathbf{E} = -\frac{1}{c} \frac{\partial \mathbf{B}}{\partial t} \quad (6)$$

$$\nabla \times \mathbf{B} = \frac{1}{c} \frac{\partial \mathbf{E}}{\partial t} + \frac{4\pi}{c} \mathbf{J} \quad (7)$$

We then take the curl of both sides of eq. 6, and with some manipulations, arrive at eq. 8.

$$\begin{aligned} \nabla \times (\nabla \times \mathbf{E}) &= -\frac{1}{c} \nabla \times \frac{\partial \mathbf{B}}{\partial t} \\ \nabla \times (\nabla \times \mathbf{E}) &= -\frac{1}{c} \frac{\partial}{\partial t} (\nabla \times \mathbf{B}) \\ \nabla \times (\nabla \times \mathbf{E}) + \frac{1}{c} \frac{\partial}{\partial t} \left(\frac{1}{c} \frac{\partial \mathbf{E}}{\partial t} + \frac{4\pi}{c} \mathbf{J} \right) &= 0 \end{aligned} \quad (8)$$

We then Fourier transform eq. 8.

$$0 = ik \times \left(ik \times \tilde{\mathbf{E}} \right) - \frac{i\omega}{c} \left(\frac{4\pi}{c} \mathbf{J} - \frac{i\omega}{c} \tilde{\mathbf{E}} \right) \quad (9)$$

Using the fact that $\mathbf{J} \propto \tilde{\mathbf{E}}$, shown in the following derivation, one arrives at equation 12.

$$\begin{aligned} \mathbf{F} &= m\mathbf{a} \\ m_e \dot{\mathbf{v}}_e &= -e\mathbf{E} \end{aligned}$$

Applying a Fourier transform to this equation results in:

$$\begin{aligned} m_e \mathbf{v}_e &= \frac{e\tilde{\mathbf{E}}}{i\omega} \\ \mathbf{v}_e &= \frac{-ie\tilde{\mathbf{E}}}{\omega m_e} \end{aligned} \quad (10)$$

Remembering the definition of \mathbf{J} and using equation 10, one gets equation 11.

$$\begin{aligned} \mathbf{J} &= -n_e \mathbf{v}_e \\ \mathbf{J} &= \frac{ie^2 n_e}{\omega m_e} \tilde{\mathbf{E}} \end{aligned} \quad (11)$$

Using the above relation, one gets equation 12 from equation 9.

$$\begin{aligned} &= -(ik)^2 \tilde{\mathbf{E}} - \frac{i\omega}{c} \left(\frac{4\pi ie^2 n_e}{\omega c m_e} \tilde{\mathbf{E}} - \frac{i\omega}{c} \tilde{\mathbf{E}} \right) \\ &= k^2 c^2 \tilde{\mathbf{E}} + \omega_{pe}^2 \tilde{\mathbf{E}} - \omega^2 \tilde{\mathbf{E}} \end{aligned} \quad (12)$$

Where ω_{pe} is the plasma frequency, defined as:

$$\omega_{pe} \equiv \sqrt{\frac{4\pi e^2 n_e}{m_e}} \quad (13)$$

Solving for ω^2 gives us the wave dispersion relation, eq 14.

$$\omega^2 = \omega_{pe}^2 + k^2 c^2 \quad (14)$$

Using the definitions of the index of refraction, N , and the speed of light in a medium, v_ϕ :

$$N \equiv \frac{c}{v_\phi} \quad (15)$$

$$v_\phi \equiv \frac{\omega}{k} \quad (16)$$

$$N = \frac{kc}{\omega} \quad (17)$$

we can take equation 14 and get equation 20.

$$\begin{aligned} 1 &= \frac{\omega_{pe}^2}{\omega^2} + \frac{k^2 c^2}{\omega^2} \\ \frac{k^2 c^2}{\omega^2} &= 1 - \frac{\omega_{pe}^2}{\omega^2} \\ N^2 &= 1 - \frac{\omega_{pe}^2}{\omega^2} \end{aligned} \quad (18)$$

Applying a geometrical optics (WKB) (Hutchinson, 1987) solution to this situation, one can find the phase lag due to the difference of the arms of the interferometer:

$$\Delta\phi = \int (k_{plasma} - k_0) dl \quad (19)$$

$$\Delta\phi = \int (N - 1) \frac{\omega}{c} dl \quad (20)$$

Defining the cutoff density n_c as the density of plasma at which our selected wavelength of light is too long to effectively penetrate the plasma. This is a constant with a given wavelength of light, using 632.8 nm in the following equation.

$$n_c \equiv \frac{m_e \omega^2}{4\pi e^2} = 2.788 \times 10^{21} \text{ cm}^{-3} \quad (21)$$

We can now solve for the phase shift as a function of plasma density (eq 22).

$$\begin{aligned} \Delta\phi &= \int (N - 1) \frac{\omega}{c} dl \\ &= \frac{\omega}{c} \int \left(\left(1 - \frac{n_e}{n_c} \right)^{\frac{1}{2}} - 1 \right) dl \end{aligned}$$

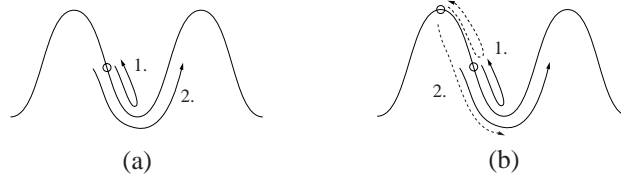


Figure 8: Intensity of interferometer output. Homodyne interferometry (a) enables measurement of the phase shift, but still leaves ambiguity of the sign of $\Delta\phi$. Certain shifts appear the same as in (1) and (2) from a detector standpoint. Heterodyne techniques (b) allow one to use two detectors, 90° out of phase, enabling one to measure the phase shift direction by correlating the data from the two detectors. (Circles represent detectors.)

Since our cutoff density n_c is so much larger than our value for n_e ($\sim 10^{14} \text{ cm}^{-3}$), we can make an approximation here.

$$\begin{aligned}\Delta\phi &\approx \frac{\omega}{c} \int \left(1 - \frac{1}{2} \frac{n_e}{n_c} - 1\right) dl \\ \Delta\phi &\approx \frac{\omega}{2n_c c} \int n_e dl\end{aligned}\quad (22)$$

Equation 22 shows that the electron density of a plasma can be calculated if one knows the length of the path being integrated over and the phase shift. The output of the interferometer allows us to measure the phase shift as a function of the light intensity of the interference pattern. However, some thought must go into exact methods of detecting the output.

As one can see from figure 8, not all detector placements are created equal. To get the most contrast and best response out of a detector, it is necessary to place it at the 90° or 270° phase difference point. This is where the change in fringe intensity in either direction is approximately linear. If one places the detector at the in phase or 180° out of phase points, one does not get a linear response. This issue however is irrelevant with our setup; we opted to use a dual detector quadrature method described in Section 3.3.

3.3 Heterodyne Interferometry

Unfortunately, the process described above leaves some ambiguity in results. When the phase shift changes from a minimum (0°) or a maximum (180°), one doesn't know the sign of $\Delta\phi$ (see figure 8a).

The solution to this type of problem is to use a heterodyne² interferometer. This technique requires two detectors 90° out of phase with each other, so that whenever one of the detectors is giving ambiguous results, the other detector reports the direction of the phase shift.

This 90° phase shift is easy to obtain when using an interferometer that is slightly misaligned

²As opposed to homodyne interferometry. Heterodyne interferometers are also known as quadrature interferometers

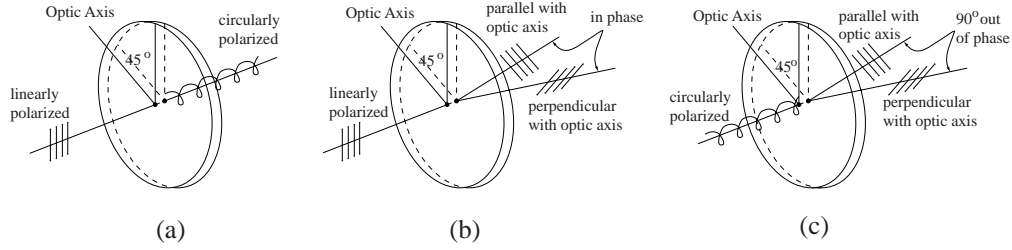


Figure 9: (a) A quarter waveplate takes a linearly polarized beam of light and circularly polarizes it. (b) The Wollaston prism takes a linearly polarized beam and splits into two orthogonal linearly polarized beams which are in phase with each other. (c) The Wollaston takes a circularly polarized beam and splits it into two orthogonal linearly polarized beams which are 90° out of phase.

which produces a pattern of many fringes. To achieve the 90° separation of the two detectors, one merely places them at appropriate places, much like in figure 8b.

If one is using a more closely aligned interferometer whose output only spans one fringe or less, one must find another method in achieving two separate outputs that are 90° out of phase with each other. One way to do this is with the use of clever optics that take advantage of the characteristics of polarized light (Buchenauer and Jacobson, 1977).

The first specialized optic that one needs in order to accomplish this is a quarter waveplate. A quarter waveplate takes a linearly polarized input, and due to the material of the waveplate, it transmits the ordinary and extraordinary components (which are defined by the orientation of the waveplate) of the input at different velocities. This causes an output which is circularly polarized, i.e. the electric field vector traces out a circle in the plane perpendicular to the direction of motion of the beam (figure 9a). This waveplate is put in the path of the reference beam. The scene beam is left linearly polarized. The two beams are recombined at the final beam splitter and then sent through the second specialized optic, a Wollaston prism. A Wollaston prism takes the ordinary and extraordinary components of the input and splits them. The Wollaston prism splits the linearly polarized scene beam into two components, which interfere with the two components resulting from the Wollaston prism splitting the reference beam. However, the two components of the scene beam are in phase with each other (figure 9b), while the two components of the reference beam are 90° out of phase with each other (figure 9c). Thus, the Wollaston produces two outputs, R_1 and R_2 , with interference occurring separately at each output between the scene and reference beams, 90° out of phase.

$$R_1 = k \sin \phi \quad (23)$$

$$R_2 = k \cos \phi \quad (24)$$

Where k is the fringe envelope amplitude.

$$k = (R_1^2 + R_2^2)^{\frac{1}{2}} \quad (25)$$

In order to analyze this output, one merely needs to solve these equations for ϕ .

$$\phi = \arctan\left(\frac{k \sin \phi}{k \cos \phi}\right) + \frac{n\pi}{2} = \arctan\left(\frac{R_1}{R_2}\right) + \frac{n\pi}{2} \quad (26)$$

Normal homodyne interferometers are not capable of measuring k . Thus when it fluctuates, there is no way of separating its effects on the output from the phase induced change. Not only is this method of quadrature interferometry capable of measuring k , the phase shift calculation ϕ is conveniently independent of k .

The above procedure works adequately when one knows that at $t = 0$, clear *sin* and *cos* outputs are available, meaning that one signal is zero and the other is at maximum. It is also sufficient when the shift caused by a phase offset, possibly caused by noise, vibration, and/or thermal drift, is small compared to the overall phase shift, such as the case of the gas calibration technique, discussed in Appendix C. Unfortunately, in the case of measuring the density of plasma in SSX, the expected fringe shift for the plasma is small, and the error introduced by an unknown phase offset becomes more of a factor. Thus, an alternative method for analysis is needed that takes into account any random phase offset at $t = 0$.

As a result, one must carefully measure the initial amplitude of each of the detector outputs before taking measurements. These initial values are measured by acoustically disturbing the apparatus and measuring the resulting signal. The signal depends on both a constant (k_1 and k_2), determined by sensitivity of the detector and intensity of the light, and the phase of the interferometer output, as seen in equations 27 and 28.

$$V_1 = k_1 \sin \phi \quad (27)$$

$$V_2 = k_2 \cos \phi \quad (28)$$

As soon as plasma enters the path of the beam, a phase change is induced ($\Delta\phi$) which changes the outputs of the detectors, as seen in equations 29 and 30.

$$\Delta V_1 = k_1 \sin(\phi + \Delta\phi) - k_1 \sin \phi \quad (29)$$

$$\Delta V_2 = k_2 \cos(\phi + \Delta\phi) - k_2 \cos \phi \quad (30)$$

By summing the squares of the detector outputs and dividing through by the appropriate k , one arrives at a fairly simple expression involving the phase change ($\Delta\phi$), as seen in equation 31.

$$\begin{aligned} \left(\frac{\Delta V_1}{k_1}\right)^2 + \left(\frac{\Delta V_2}{k_2}\right)^2 &= [\sin(\phi + \Delta\phi) - \sin \phi]^2 + [\cos(\phi + \Delta\phi) - \cos \phi]^2 \\ &= 2[1 - \sin(\phi + \Delta\phi) \sin \phi - \cos(\phi + \Delta\phi) \cos \phi] \\ &= 2(1 - \cos \Delta\phi) \end{aligned} \quad (31)$$

One can perform relatively simple manipulations on equation 31 and arrive at equation 32.

$$\Delta\phi = \cos^{-1} \left[1 - \frac{1}{2} \left[\left(\frac{\Delta V_1}{k_1}\right)^2 + \left(\frac{\Delta V_2}{k_2}\right)^2 \right] \right] \quad (32)$$

In this manner, one can calculate the phase shift induced by the plasma if the output of the detectors is known as a function of time and their amplitude ranges.

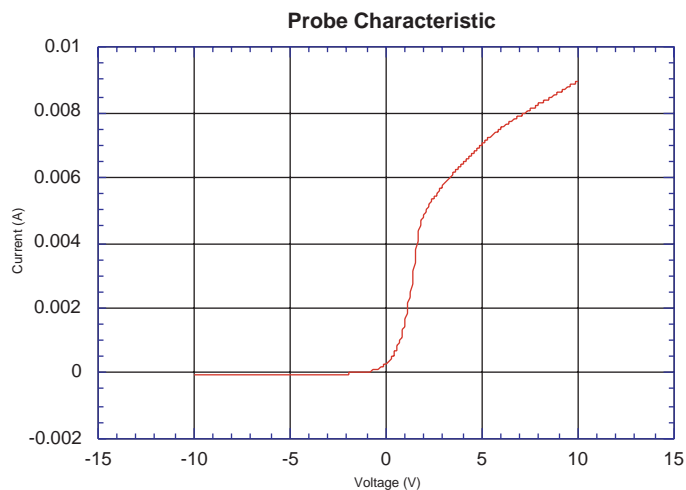


Figure 10: A typical graph of the probe characteristic of a Langmuir probe, obtained in SSX’s calibration device.

4 Langmuir Probe

4.1 The Simple Langmuir Probe

The Langmuir probe is one of the simplest possible diagnostics to construct for obtaining measurements of plasma. The probe is constructed out of a conducting material and housed in a sheath capable of withstanding the heat of the plasma. In operation, one applies a voltage bias to the probe. This voltage induces a current, composed of ions or electrons, depending on the bias. When this voltage is below that of the plasma, ions are collected; when the voltage V is above the plasma potential ϕ_p , the probe collects electrons, and the current is positive.

The ion saturation current i_+ and electron saturation current i_- occur when the probe tip is biased at a large enough value so that all accessible electrons or ions in the surrounding area are being attracted to the tip of the probe. This saturation current is much higher for the electrons, mainly due to mass differences between ions and electrons.

When the probe is biased higher than the plasma potential, $V > \phi_p$, the electron saturation current is given by equation 33 (Ji et al., 1991).

$$i_- = \frac{1}{4} A_- e_- n_e \sqrt{\frac{8T_e}{\pi m_e}} \quad (33)$$

If the probe bias is lowered past the plasma potential, the Boltzmann factor is added to the electron current, as seen in equation 34.

$$i_- = \frac{1}{4} A_- e_- n_e \sqrt{\frac{8T_e}{\pi m_e}} e^{-e(\phi_p - V)/kT_e} \quad (34)$$

When electrons are no longer being collected by the probe, one has reached the ion saturation current. The saturation current density for the ions is given by the ion density near

the probe times the ion charge times the velocity of the ions, which is near the sound speed C_s (Cohen, 1995). Multiplying by the surface area of the probe tip, we arrive at equation 35 for the ion saturation current.

$$i_+ = A_+ e_- n_e C_s \quad (35)$$

$$C_s = \left(\frac{\gamma Z k T_e}{m_i} \right)^{\frac{1}{2}} \quad (36)$$

A_+ and A_- denote the ion and electron gathering area on the probe. These are essentially equal to each other and are determined by the construction of the probe. C_s is the ion sound speed.

In general, the above equation for the ion saturation current is for large planar probes. Small cylindrical probes are used in SSX and in general, they are more common in the study of plasma. Thus, equation 35 is modified by an extra term ($e^{-\frac{1}{2}}$), as shown in the following equation.

$$i_+ = e^{-\frac{1}{2}} A_+ e_- n_e C_s \quad (37)$$

These two saturation currents determine what is called the probe characteristic, given in equation 38. A typical probe characteristic appears in figure 10.

$$I_p = \begin{cases} -i_+ + i_- e^{-e(\phi_p - V)/kT_e} & V \leq \phi_p \\ i_- & V \geq \phi_p \end{cases} \quad (38)$$

One can fit equation 38 to the plot of the probe characteristic to arrive at values for the electron density n_e and electron temperature T_e . The problem with using a Langmuir probe to make this measurement is that one must scan a range of voltages to measure the current drawn on the probe. This unfortunately takes more time to take a measurement than allowed in an experimental environment such as SSX. An alternative to the regular Langmuir probe that allows one to measure time-varying plasmas is the triple probe (Ji et al., 1991).

4.2 The Triple Probe

The triple probe is an assemblage of three Langmuir probes connected in a particular way, illustrated in figure 11. The following analysis follows Ji et al. (1991). P_2 measures the floating potential of the plasma V_f . The floating potential is the voltage measured when no current flows through the probe with very high impedance. V_{d2} is the potential difference between P_1 and P_2 . V_{d3} is a constant voltage applied between probe tips 1 and 3 (P_1 and P_3). This induces a current to flow from the plasma through P_3 and out P_1 , denoted by I_1 , which is equivalent to the ion saturation current. Using equation 38, one can calculate the current running through the three probes, finding:

$$-I_1 = -i_- e^{-\frac{V_1}{T_e}} + i_+ \quad (39)$$

$$0 = -i_- e^{-\frac{V_2}{T_e}} + i_+ \quad (40)$$

$$I_1 = -i_- e^{-\frac{V_3}{T_e}} + i_+ \quad (41)$$

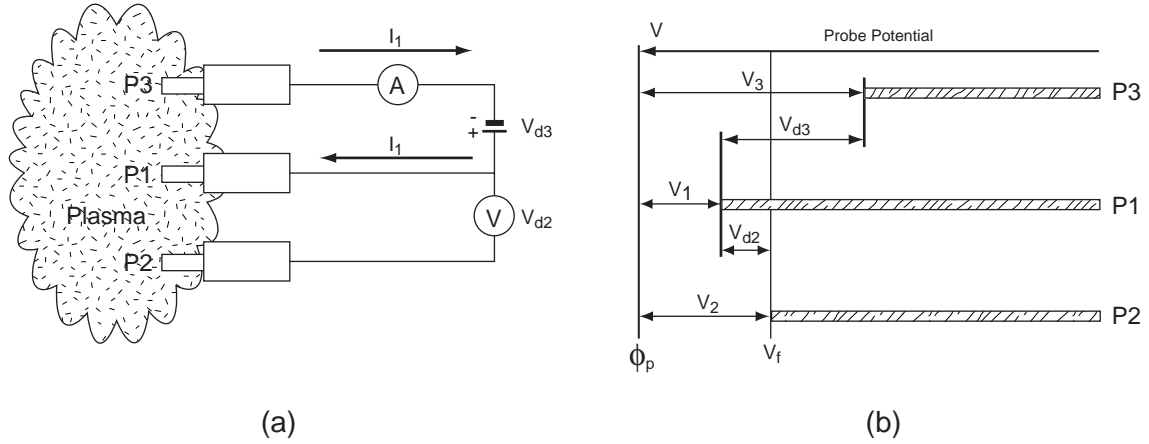


Figure 11: (a) Circuit for triple probe and (b) potential diagram for triple probe.

where V_i is the voltage difference of the i th tip and ϕ_p .

Using these equations and the definitions of $V_{d2} = V_2 - V_1$ and $V_{d3} = V_3 - V_1$, one arrives at equations 42 and 43 (Ji et al., 1991).

$$\frac{1}{2} = \frac{1 - e^{-\frac{V_{d2}}{T_e}}}{1 - e^{-\frac{V_{d3}}{T_e}}} \quad (42)$$

$$i_+ = \frac{e^{-\frac{V_{d2}}{T_e}}}{1 - e^{-\frac{V_{d2}}{T_e}}} \quad (43)$$

Plotting these two equations as a function of V_{d2} and with different values of V_{d3} , one gets the graphs in figure 12. In the region $T_e < V_{d3}/2$, the curves for specific values of V_{d3} are mostly linear. Using this fact, one can take the limit of equation 42 in the case that $T_e \ll V_{d3}$ and get the following simple relationship:

$$T_e \approx \frac{V_{d2}}{\ln 2} \quad (44)$$

The triple probe, and all Langmuir probes, can also be used to measure density. Going back to equation 35, the equation for the ion saturation current, one can see that since i_+ is being measured, once one has calculated T_e , it is very easy to calculate the electron density.

$$n_e = \frac{e^{\frac{1}{2}}}{A_+ e_-} \sqrt{\frac{m_i}{\gamma Z k T_e}} \quad (45)$$

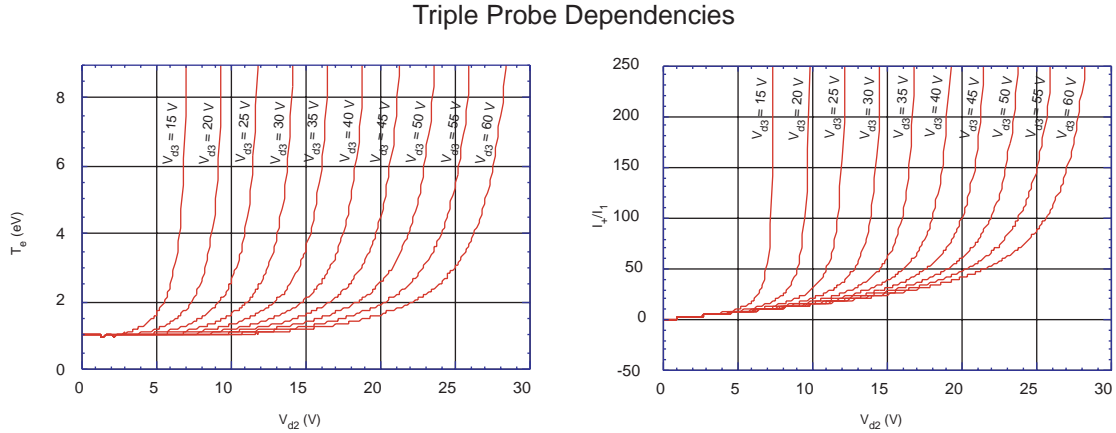


Figure 12: The triple probe’s measurements are dependent on the value of V_{d2} used. The lines on each graph correspond to different values of V_{d3} . The graph on the left shows the dependency of T_e on V_{d2} , while the second graph shows I_+/I_1 . Notice the fact that the curves are linear in the region $T_e < V_{d3}/2$.

5 Experimental Setup

5.1 Physical Dimensions

The experimental environment of SSX is illustrated in figure 14 on page 18. The vacuum chamber is a barrel shaped container one meter in length, shown in gray in figure 14, that subdivided by the two flux conservers, shown in black. Each flux conserver has a radius of $r_{cons} = 25.4$ cm and has a length $L_{cons} = 30.8$ cm. Two coaxial spheromak guns are mounted on the vacuum vessel, one on each end of the chamber. The guns have radius of $r_{gun} = 8.41$ cm.

The two flux conservers are separated by a 2.5 cm gap, which is the plane of reconnection. This gap is a channel for any particles accelerated out of the reconnection region to exit the area without interference from the magnetic field or neutral gas from the plasma of the spheromaks. Also visible on figure 14 are chevron-shaped cutouts, approximately 10 cm by 5 cm, in the flux conserver wall bisecting the machine. These cutouts are the actual sites of interaction and reconnection between the two spheromaks. The cutouts allow for a partial interaction to occur while still preventing the two spheromaks from completely merging. These cutouts also serve the function of localizing the interaction in these two regions, allowing instruments to be focused in only one or two spots.

Diagnostic instrumentation can be installed at various points along the vessel. Three large ports are accessible, one on the top and two on the sides. The fourth of these is occupied by the cryo-pump needed to maintain the vacuum. These large ports all lie on the perimeter of the reconnection plane. One of these ports is used for the upcoming three dimensional magnetic probe array (Schlossberg, 2001), which records over 600 channels of data. The top port is used as a stage for several smaller instruments which are aimed at the reconnection

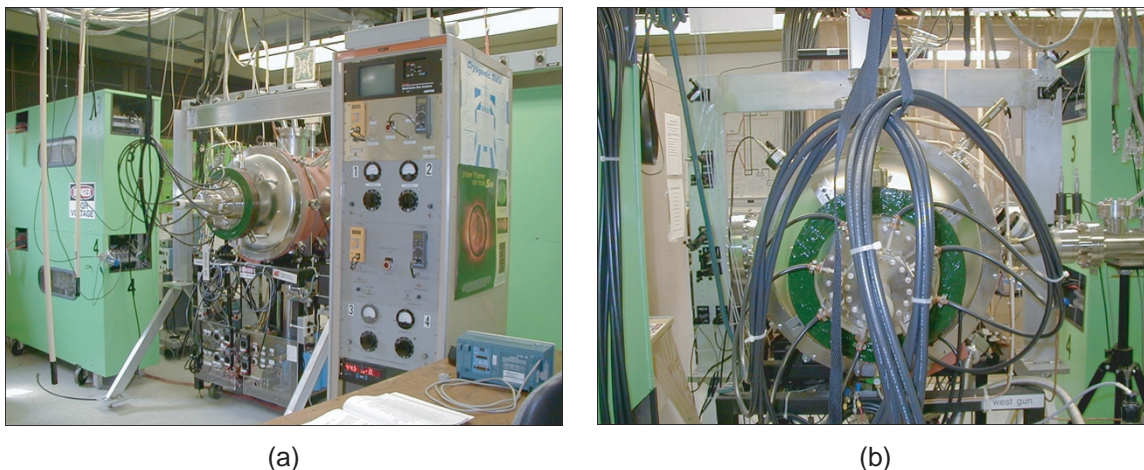


Figure 13: (a) shows the east side of SSX. The back of the interferometer yoke can be seen clearly. (b) shows the west side of SSX. The triple probe is the brass instrument on the upper right side of the vacuum chamber. The interferometer optics can be seen on the yoke, with the waveplates, Wollaston prism, and detectors on the left side.

region. These instruments document the energetic particles coming out of the reconnection region.

Smaller ports are also located on the machine. There are eight located on the perimeter of the middle of each flux conserver, and an additional four more are located in the same plane as the large ports. These smaller ports are host to a couple of valves for pumping down the machine and several diagnostics, including a monochromator, a particle analyzer, a photon analyzer, a triple probe (described in section 4), and lastly, the entrance and exit windows for the HeNe interferometer. The windows used for the interferometer are made out of fused silica, providing better than 90% transmission. Both the triple probe and the interferometer are located out of the plane of reconnection, allowing measurements to be made only on the noninteracting part of the spheromak.

5.2 Operating Parameters

SSX is operated within a certain optimal range of parameters for the discharge of the capacitor banks attached to the coaxial spheromak gun and for the stuffing flux of the gun. This optimal range was determined from the study of Kornack (1998).

Typical gun parameters are $V_{gun} = 5\text{kV}$ and $B_{stuff} = .9\text{mWb}$. A typical shot appears in figure 15. Varying the delay that triggers the capacitor bank discharge effectively changes the stuffing flux. This is because the plasma generated by the capacitor bank discharge encounters the stuffing field at a different time in the stuffing field's strength. This relationship is shown in figure 16.

During the typical “run,” we take data for only $250\ \mu\text{s}$. The first $50\ \mu\text{s}$ of the data is an empty buffer right before the “shot.” Time $t = 0\ \mu\text{s}$ is set as the discharge of the capacitor

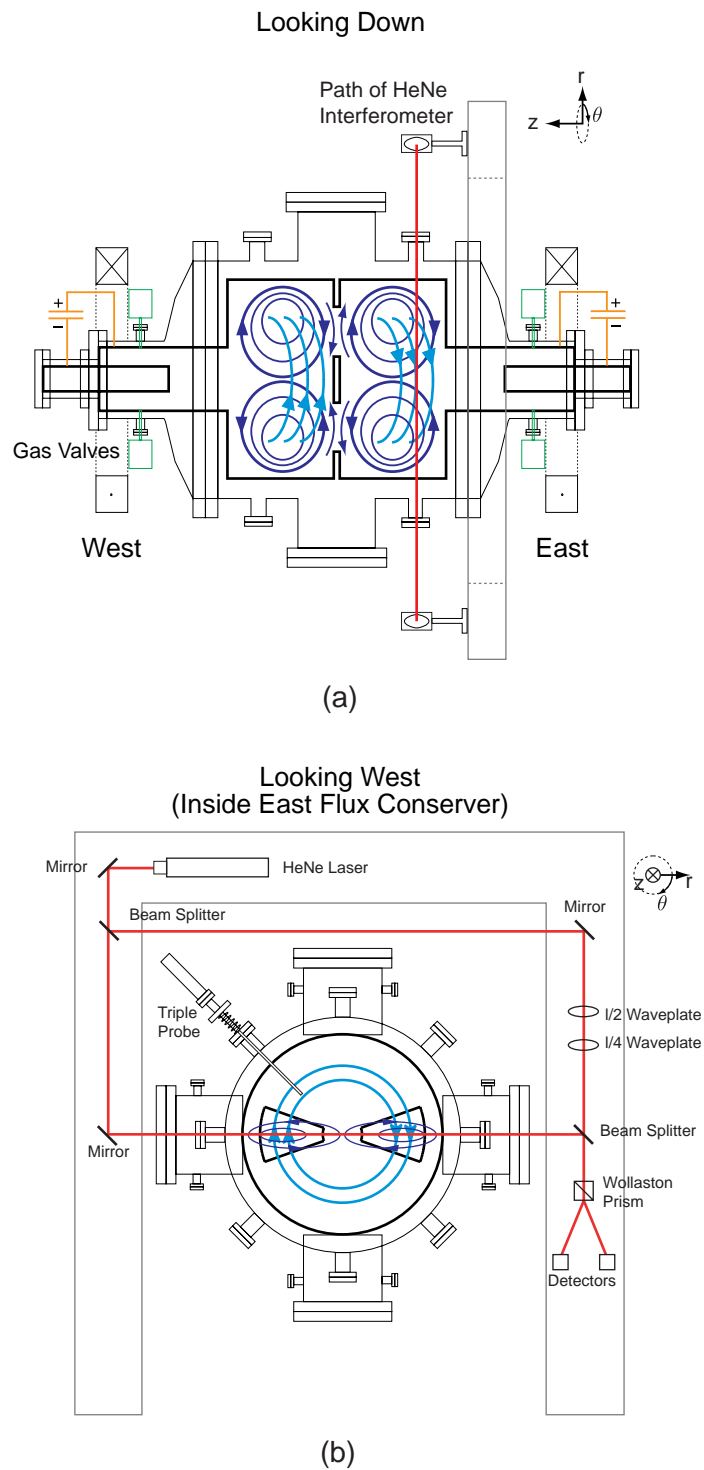


Figure 14: A schematic of the experimental apparatus from the (a) top and from the (b) east side.

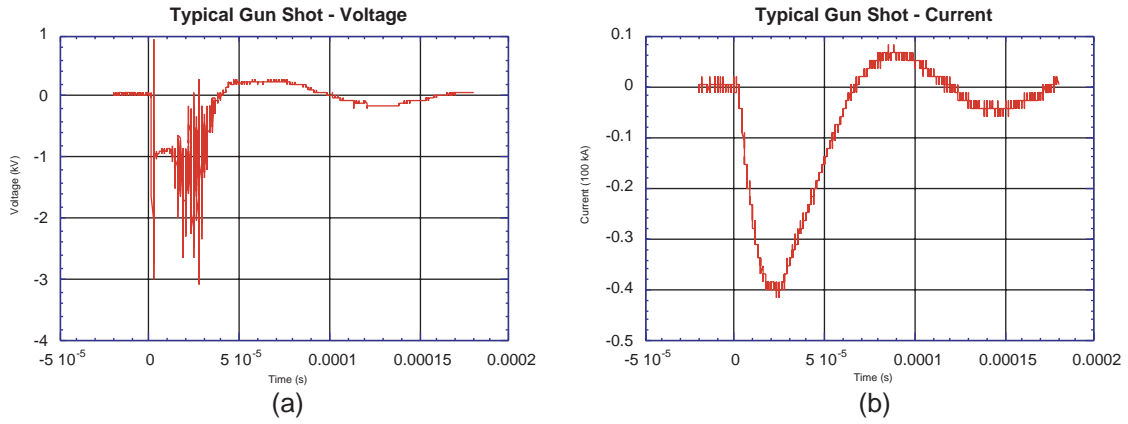


Figure 15: A typical gun shot is shown in the graphs above. (a) depicts the voltage on the capacitor bank which discharges into the gun, while (b) shows the current.

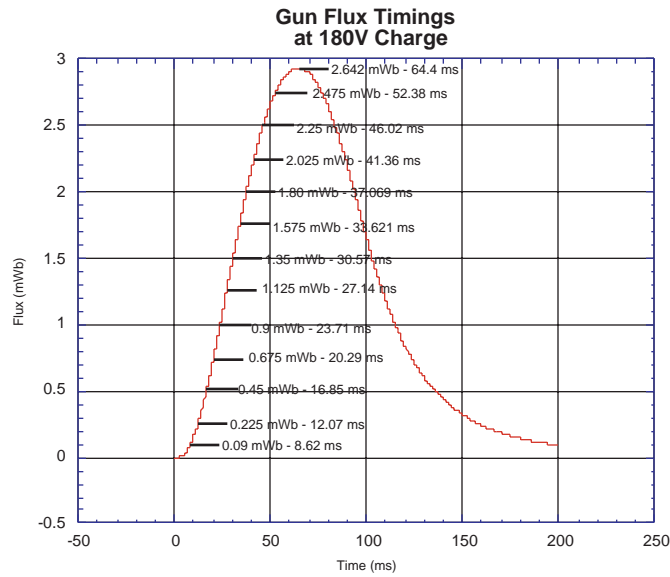


Figure 16: This graph shows the relationship between the delay on the capacitor bank trigger and the effective stuffing field.

Density	$n_e \approx n_i$	10^{14} cm^{-3}
Temperature	$T_e \approx T_i$	15 eV
Magnetic Field	B_{typical}	500 G (1000 G max.)
Beta	β	10%
Alfvén speed	v_{Alf}	10 cm/ μs
Lundquist Number	S	< 1000
Electron skin depth	c/ω_{pe}	0.5 mm
Ion skin depth	c/ω_{pi}	2.3 cm
Larmour radius	ρ_i	0.9 cm
Sweet-Parker thickness	δ_{S-P}	0.15 cm ($L' = 10 \text{ cm}$)
Collisionless thickness	δ_C	4.6 cm

Table 1: SSX Plasma Parameters

banks. The spheromak formation occurs between $t \approx 15 \mu\text{s}$ and $t \approx 40 \mu\text{s}$. We record data for an additional $160 \mu\text{s}$, though most of interesting physics occurs early on, and by $t \approx 170 \mu\text{s}$, the spheromak has dissipated to the point of being unmeasurable.

Typical plasma characteristics are summarized in table 1.

5.3 Interferometer Construction

As mentioned in section 3, the HeNe interferometer used on SSX is based on the Mach-Zehnder design. The interferometer uses several specialized optics not normally found in Mach-Zehnder interferometers; the use of these is discussed in section 3.3. The exact specifications of the components used in the interferometer designed by the author are discussed in appendix B.

Normally an interferometer of this sort would be mounted on an acoustically isolated optical bench. Such measures are necessary in order to isolate such a sensitive system from disturbances. Though a mounting arrangement like this is technically possible, it is not necessarily economic in terms of funding or in space. Fortunately, the time scale of the SSX experiment is extremely short, on the order of $100 \mu\text{s}$. At such a short duration, most acoustic disturbances are of too short a frequency to noticeably affect the interferometer. As such, using an isolated optical bench is somewhat overkill. This allows us to use a much simpler and cheaper design.

The frame used for mounting the interferometer components, which can be seen in figure 17 on page 21, is an inverted U constructed out of 6-inch U-channel. Metal plates were welded onto the legs of this frame which provide for the interface to the legs of the whole structure. Two inverted V's were constructed out of 3-inch U-channel as legs, each with square plates welded onto the legs and the apex of the V's. The apex of each V was attached to the bottom of the U-frame. The modularity of this design allows for layers of insulation (such as neoprene) to be added between the U-frame and the legs, further isolating the interferometer components if needed. Swivel feet with rubber bottoms were attached to the bottoms of the legs, providing for another layer of insulation. Each foot is adjustable in

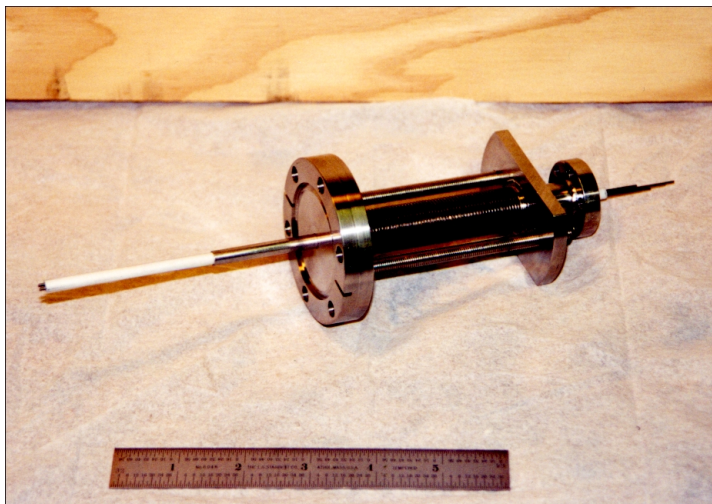


Figure 18: Illustration of the triple probe in its fully retracted position.

height so one may level the whole structure if needed.

The surface of the U-frame was strategically perforated with $\frac{1}{4}$ -20 tapped holes on 1 inch centers so that optical components could be mounted with standard optical bench mounting hardware. Tapped holes were also put in the sides of the mount. This allows for the installation of a lucite covering over the path of the beam, if needed, to isolate air currents in the future. The mock-up for the interferometer was checked for response to air currents. The overall affect of these air currents was measurable, but deemed insignificant on the SSX timescale.

All analysis was performed in Matlab. The analysis routine for the interferometer can be found in appendix D and is based on equation 32.

5.4 Triple Probe Construction

The triple probe installed on SSX consists of four Langmuir probes housed in a single body. The probe tips are arranged in a square pattern. The probe tips are constructed out of tungsten wire, 1 mm in diameter. Each tip exposes only 1 mm of the length of the wire, given a total exposed area of $A_+ = A_- = 3.6 \times 10^{-6} \text{ m}^2$. The four probes run down the same protective sheath, seen in white in figure 18. Attached to the top of the vacuum flange is a bellows that allows the probe to be moved in and out without endangering the integrity of the vacuum. Two threaded shafts ($\frac{1}{4}$ -28) control the amount that the triple probe is extended. When installed, the probe can measure anywhere from $R_{SSX} = 1$ to $R_{SSX} = .75$, defining $R_{SSX} = 1$ as the radius of the flux conserver, $r_{cons} = 25.4 \text{ cm}$. The brass housing at the top of the triple probe merely provides a mounting area for the BNC connectors.

Cabling is attached to the BNC connectors on the triple probe which runs back to the control cage. Three of these cables are attached together in the circuit shown in figure 11.

The voltage V_{d2} is measured between probe tips P_2 and P_3 by means of a Tektronix Voltage Isolator.³ I_1 is measured by a current monitor.⁴ Instead of using a traditional power supply, the applied voltage was supplied by means of a capacitor of capacitance $176 \mu\text{f}$ so as not to introduce electrical noise into the system. The capacitor was charged up to a voltage $V_{d3} = 30$ to 45 V.

The fourth probe in the triple probe housing is isolated from the other three probe tips. This probe is also attached to a Tektronix Voltage Isolator, allowing measurements of V_f to be taken.

All analysis was performed in Matlab. The analysis routine for the triple probe can be found in appendix D and is based on equations 42-45.

³Model A6909 Sony/Tektronix Two Channel Isolator.

⁴The current monitor was Pearson current monitor, model 411, with an output of .1 V per A.

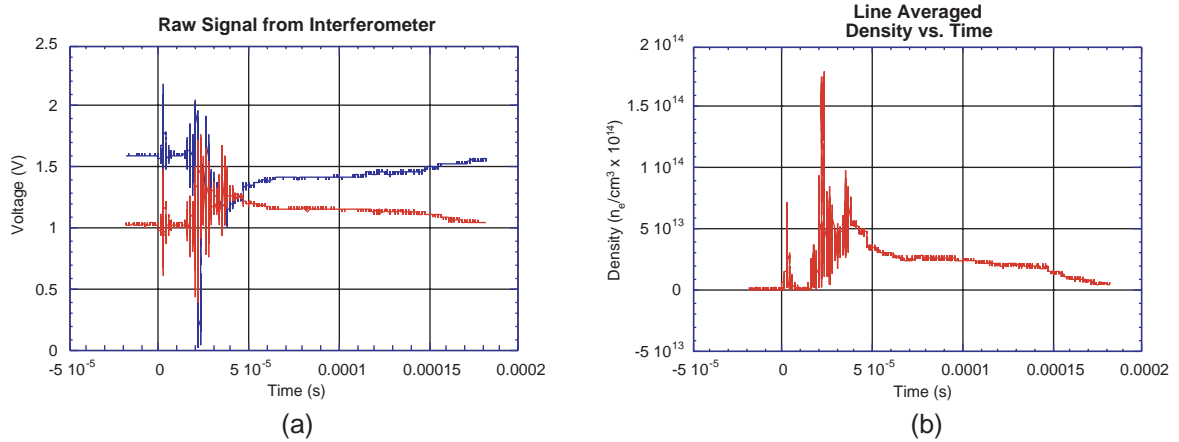


Figure 19: A typical measurement made by the interferometer. (a) shows the raw data, while (b) shows this data after analysis. The large spikes are most likely due to noise.

6 Experimental Results

6.1 Interferometer Data

Prior to any actual data taking, the mount of the interferometer is acoustically disturbed by tapping on it. This results in the output of the detectors going to their maximums and minimums. The amplitudes of these signals are recorded as k_1 and k_2 of equation 32. Figure 19a shows what the typical data from the interferometer looks like. This data is then run through the analysis routine shown in section D, giving us the output shown in figure 19b. At the beginning of the spheromak’s “life,” one can see a lot of noise and a couple of particularly high spikes. These features are due to the large amount of RF noise and $\dot{\Phi}$ generated by the spheromak formation. $\dot{\Phi}$ is the change in magnetic flux with respect to time. During formation, the $\Delta\Phi_B$ is relatively large in a short amount of time Δt , so contributions from $\dot{\Phi}$ can be large.

$$\frac{\Delta\Phi_B}{\Delta t} = \dot{\Phi} = \varepsilon \quad (46)$$

As a result of these byproducts of spheromak formation, any large narrow spikes should be considered as noise or $\dot{\Phi}$. One can see from this graph that after this period of turbulence, the density of the spheromak tops out at about $5 \times 10^{13} n_e \text{ cm}^{-3}$. A short period later, density drops off to about $2 - 3 \times 10^{13} n_e \text{ cm}^{-3}$, where it remains for a relatively long time. Near the end of the recorded data, the spheromak’s density begins to die off.

Referring back to figure 5, one can see that the amount of stuffing flux can be changed by adjusting the delay on the trigger for the capacitor banks. As described in section 2.2, this stuffing field acts as a soap bubble; when the plasma hits this field, the field distends and wraps around the plasma. To continue the analogy of a soap bubble, if one doesn’t blow hard enough on the film (if the stuffing field is too strong), the film distends a little and then bounces back, never ripping free. In this case, the soap film (stuffing field) acts like

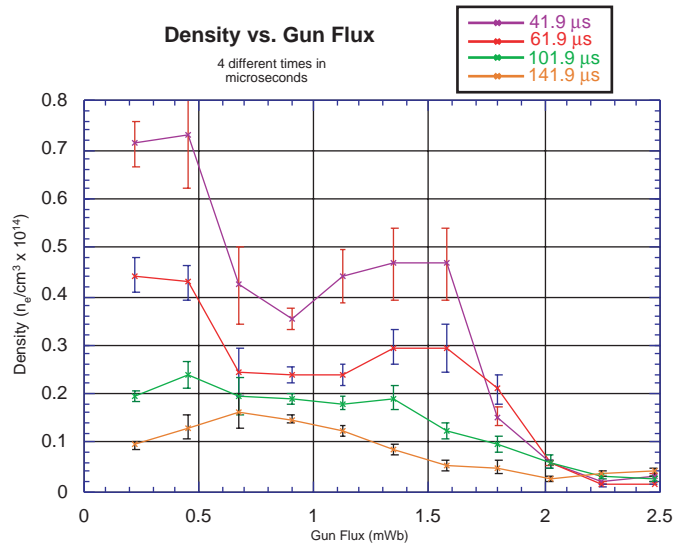


Figure 20: Each of the four traces depicts density as a function of stuffing flux on the spheromak gun. Each trace is sampled at a different time, i.e. the top trace shows the density at time $t = 41.9 \mu\text{s}$ as function of stuffing flux.

a stiff rubber band. The other extreme is if one blows too hard at the soap film (i.e. the stuffing field is too weak). In this case, the soap film blows apart. The analogous condition in a spheromak gun prevents spheromak formation. Instead, a gush of unconfined plasma is launched out of the end of the gun, not giving the stuffing field a “chance” to enclose the plasma.

In figure 16, one can see the effects on the plasma density of varying the stuffing field. The graph displays the density of the plasma as a function of gun flux. Each trace represents a different time, with the uppermost line being the earliest and ending with the bottom line. This method of graphing, though slightly unintuitive, was chosen to allow for the inclusion of error bars. It would be possible to plot several plasma densities as a function of time, each at different times, but this would not allow us to calculate mean values or error bars for the density.⁵ To see the time evolution of density at a given gun flux setting, one would hop from trace to trace. This data was taken over the course of a day, with any where from 5 to 20 shots per flux setting.

As one can see, at all flux settings, the density drops off from $41.0 \mu\text{s}$ to $141.9 \mu\text{s}$. For the low flux settings, the plasma density starts off relatively high, but the plasma rapidly dissipates. This is indicative of poorly confined plasma that is rocketing out of the end of the spheromak gun without giving a chance for the stuffing field to encapsulate it. Early on at around $.9 \text{ mWb}$ of flux, the density of the plasma is lower, but it remains relatively consistent throughout the experiment’s duration. Centered around 1.4 mWb of flux, the initial density pops back up, but at a cost to the density later on. If too much stuffing flux is applied ($\geq 1.6 \text{ mWb}$), then the stuffing field starts to act as the aforementioned “rubber

⁵Mean values and error bars were calculated in KaleidaGraph 3.5.

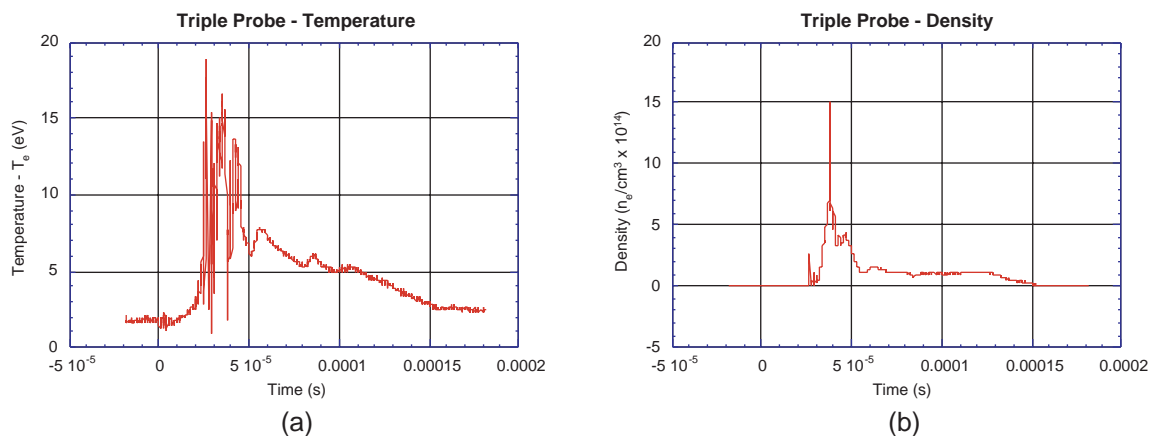


Figure 21: Typical data from the triple probe. (a) shows temperature as a function of time and (b) shows density as a function of time. Both measurements were made from a point 39.3 mm from the outer wall of SSX. This position corresponds to a radius $R_{SSX} = 0.808$.

band,” and at (≥ 2 mWb) the field completely clamps down on the plasma letting very little escape the gun. This is evident by the negligible results of density at these settings.

We choose to run SSX with a stuffing field of .9 mWb on the guns because the provides the most stable consistent spheromaks, as seen in figure 20. Though higher initial densities could be attained by adjusting the stuffing flux in either direction, sacrifices would have to be made. The spheromaks would not be as consistent in their density. The range of their densities is much greater during the course of a run, giving to the suspicion that they are less stable. Since the purpose of the stuffing field is to provide the necessary \mathbf{B} fields for confinement, we choose the setting that provides for the most stable confinement, even if that is at the cost of density.

6.2 Triple Probe Data

Typical triple probe data after analysis is shown in figure 21. This data corresponds to measurement made at a radius of $R_{SSX} = 0.808$ (39.3 mm from the outer wall) with probe bias $V_{d3} = 36.5$ V. Figure 21a shows the temperature as measured by the triple probe, while 21b displays the density. The temperature of a typical shot peaks anywhere from 10 – 15 eV and usually displays comparable stability to the shot shown in this figure. Most measurements of density also look similar to this graph. Notice the comparison between the shapes of figures 19b and 21b and how they both display the same characteristic shape. However, one can easily note that the actual measured values for n_e between the two diagnostics do *not* correspond. Langmuir probe densities are often off by some multiplicative constant (Owens, 1980). This constant can be determined by calibrating the triple probe by other means, in this case an interferometer. Even though both sides of SSX are technically identical, since the triple probe was located on the west side of SSX and the interferometer was on the east, we were unable to perform this calibration. Both diagnostics should be sampling the same plasma. This remains to be done in the future.

Figure 22 shows the results from a scan from the outer wall of SSX $R_{SSX} = 1$ down to $R_{SSX} = .75$. At each value for R_{SSX} , between 8 – 20 measurements were made. This data was analyzed and then organized according to R_{SSX} , allowing us to obtain mean values and error bars at each value of R_{SSX} .⁶ Peak values of T_e and n_e were used for these graphs. It is interesting to note that at values of $R_{SSX} \leq .9$, around 2.5 cm in from the wall, the temperature shown in figure 22a begins to level off. Whether this trend continues is unknown; a longer device is required to probe further. Interesting behavior also occurs in density shown in figure 22b. As one moves towards the center of the vacuum chamber, the density of the plasma rises, then dips, rises again, and dips one final time. What this means over all is hard to tell since we cannot measure any more deeply in the plasma, though it is interesting that a thin shell of plasma which is denser than the rest lies very close to the outer wall of the vacuum chamber. Both T_e and n_e drop to zero as they approach the wall, which is to be expected.

Figure 23 shows data from the same set as shown in figure 22. Instead of using the peak values for T_e and n_e , four different times were sampled, similar to the process used for figure 20. In this graph we can get a rough idea of how the radial profiles for T_e and n_e change with time. Not surprisingly, both values gradually fall away.

⁶Mean values and error bars were calculated in KaleidaGraph 3.5.

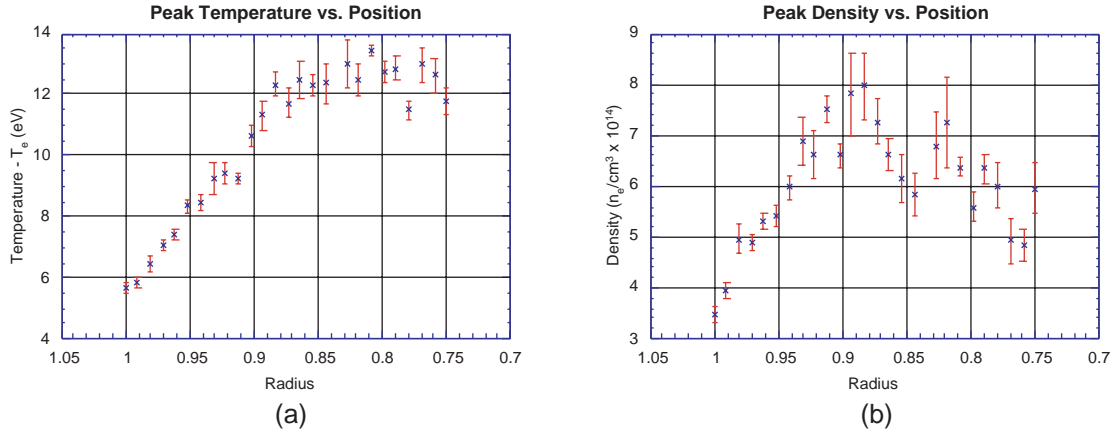


Figure 22: Radial profiles of peak (a) temperatures and (b) density occurring during a shot, as measured with the triple probe.

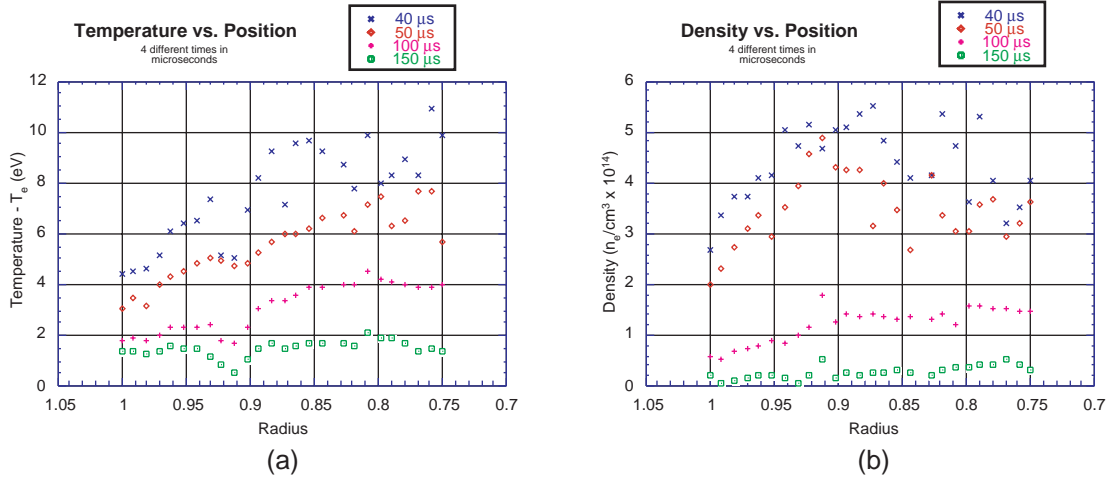


Figure 23: Radial profiles of peak (a) temperatures and (b) density occurring during a shot, as measured with the triple probe. Each trace shows the temperature or density at a different time, i.e. the top trace is for time $t = 40 \mu\text{s}$.

7 Future Directions

SSX is anticipating exciting directions in the near future. A three-dimensional magnetic probe is nearing completion which will measure over 600 channels of data from the interaction region where the two spheromaks reconnect. This probe is the next in the progression from the linear and 2D probes detailed in Kornack (1998). Other new directions in the area of diagnostics includes a newly completed AXUV device for measuring soft x-rays, discussed in Schlossberg (2001).

Pertaining to the topic of this thesis, the most important action to be taken in the future is to finally calibrate the triple probe with the interferometer. Once both diagnostics are up and running on the same side, a more detailed study of the physical nature of the spheromaks can be pursued. Other suggested experiments include comparing n_e to $H\alpha$, measured by the DD3 detector, and a comparison of the plasma density before and after the conversion of the capacitor banks. The conversion will double the capacitance, which should lengthen the lifespan of the spheromak by approximately $\times\sqrt{2}$. One last study would be to compare simulation data, as described in Lukin (2000), to the line-averaged results of n_e from the interferometer and the radial profiles of both T_e and n_e from the triple probe.

Once this suite of diagnostics is completed and fully tested out, SSX will begin its next phase of experimental operations where dividing walls between the flux conservers will be removed. This will allow for the two colliding spheromaks to fully merge. Other measures will be taken, including installing the necessary external coils needed to supply the stabilizing \mathbf{B} fields, which will convert the two merging spheromaks into a Field Reverse Configuration (FRC).

Appendix A: Interferometer Setup

This section will detail how to setup and align the interferometer. The interferometer is easiest to setup when working from the beginning of the optical path and setting up each component in the order that the beam encounters them. If set up in proper order, there should be no reason to be tinkering with more than two components at a time: the ones located at each end of the beam path that you are currently aligning.

As a result, the laser is the first part that needs to be setup. It is helpful to make sure that the laser is oriented parallel to the working surface. Aim the laser at the center of the beam steering mirror (component M1 in figure 24) and rotate the laser barrel so that its plane of polarization makes $\approx 45^\circ$ angle with the working surface. A polarizer is handy during this step.

Once the laser is set up, reflect the beam at a 45° angle onto the first beam splitter (BS1). Again, try to aim the beam at the center of the beam splitter; this will make later fine tuning much easier. If 2" optics are used, it is less important to target the centers of the optics than if 1" optics are used.

At this point, make sure the laser beam is aimed at the center of the scene beam mirror (M2). This is the mirror that is in the path of the laser which is transmitted through the first beam splitter (BS1). Then aim the beam splitter so that the reflected portion of the split beam hits the center of the reference beam mirror (M3). Then the two mirrors should be positioned so that they in turn reflect their beam to the center of the final beam splitter (BS2). This is an important step. One should be sure that both beams incident on the final beamsplitter (BS2) are aimed at the *same point* on the surface of the beamsplitter that is closest to the output of the interferometer that you are using. There should be two outputs of the interferometer at this point; one is generally not used at and in our specific setup; it is completely ignored. Thus, the beam that is transmitted through the final beamsplitter (BS2) should exit at the point that the reflected beam hits the final beam splitter. At this point, the last step to take is to aim the final beamsplitter so that the reflected beam is aimed at the same spot that the transmitted beam is aimed at.

Now that the basic interferometer is established, one can start looking for interference patterns. It is handy to use an objective lense at this stage so that the interference patterns are easy to see with the naked eye. The easiest way to locate interference patterns is to tweak the final beamsplitter's (BS2) tilt about the vertical axis using the provided adjuster on the back. This is the adjuster that is located on the end of the bottom of the optic mount, not the adjuster on the corner⁷. One notices that as the interferometer gets closer to alignment, the fringes get larger until the output of the interferometer is dominated by one large fringe. During this process, it is useful to adjust the angle of the fringes so that they are aligned vertically by using the adjuster at the top of the mount. This adjuster tilts the mount about a horizontal axis. By a combination of the two adjusters one can trace out the traditional bullseye interference pattern. However, our use of the instrument requires the interferometer to be set at a point where only one fringe, or a fraction thereof, is seen

⁷This adjuster translates the whole mount in a direction perpendicular to the plane of the optic.

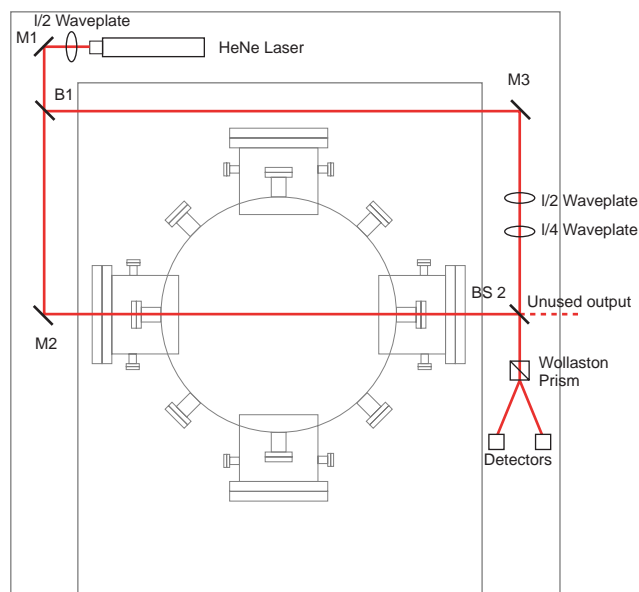


Figure 24: Basic layout of SSX interferometer.

at the output.

Once the desired output is achieved, the next step is to adjust the optics necessary to produce a second output beam 90° out of phase with the original beam. Place the Wollaston prism at the output of the interferometer, aligned so that its optical axis is horizontal to the working surface. This should produce a two-beam output. The alignment of the Wollaston prism is correct when the two output beams lie in a plane parallel to the working surface. Place the two detectors in their positions.

Block the reference beam at this point and monitor the output of the detectors placed at the Wollaston output. Rotate the angle of the laser, changing the plane of polarization so that the Wollaston prism evenly divides the scene beam, producing the same signal in each detector. Unblock the reference beam and block the scene beam.

Place the $\frac{\lambda}{4}$ plate in the reference beam. Make sure that its orientation, denoted by the marking on the optic which is labeled “fast,” is horizontal to the working surface and makes a $\approx 45^\circ$ with the plane of polarization of the laser beam. Place the $\frac{\lambda}{2}$ plate after the first beam splitter in the reference beam, but before the $\frac{\lambda}{4}$ plate. This will allow precise alignment of the plane of polarization of the laser beam entering the $\frac{\lambda}{4}$ plate. Adjust the angle of the $\frac{\lambda}{2}$ plate by loosening the thumbscrew on the rotation stage and adjusting the angle of the stage by hand. Tighten the thumbscrew and then make fine adjustments using the micrometer adjuster. Adjust until the signal in the two detectors is the same.

The interferometer should now generate two output beams which are 90° out of phase with each other. Check this by inspecting the output of the detectors on an oscilloscope. In order to do this, center each trace on the screen. One easy way to do this is to turn on only one trace and tap the interferometer yoke. This will produce a signal that should touch both

boundaries of the signal. Center this and repeat for the other channel. Once this is done, let the interferometer sit for several seconds and examine the output. When one signal crosses the midline, the other trace should be reaching either a minimum or maximum. If this is the case, then you are finished. If not, fine tune the $\frac{\lambda}{2}$ plate until this occurs. The interferometer should now be complete.

Appendix B: Component Specifications

Since interferometry is such a sensitive measuring tool, it is necessary to obtain relatively high quality components. Interferometers are often used to find defects in lenses; this illustrates the sensitive device it really is. As a result one must be careful of the grade of components used. In selecting the components used for our instrument, we took in to account optical quality, ease of use, and stability. We ordered primarily from Newport Corporation, Coherent, and Thorlabs Inc. for the optical hardware, UDT Sensors, Inc. for the sensors, and ISI for the vacuum viewports. A complete model list is included at the end of this section.

All component specifications were reached after extensive testing on a mock-up interferometer built on an optical bench with previously available components. After this testing phase, specific components were settled on and ordered. A second testing phase was entered using the newly procured parts. During this period, the gas density calibration described in section C was performed, as well as the designing of the mounting yoke described in section 5.3.

All the optical mounting hardware, including posts, post holders, bases, and optic mounts were obtained from Thorlabs. Their Ultrastable Kinematic optical mounts provided the most stable and affordable solution while still giving us fine control over translation⁸ and tilt about the horizontal and vertical axes. Posts and post holders used were of the regular 3" variety. For the most flexibility in placing each optic, we ordered the large bases from Thorlabs, which come predrilled for many mounting possibilities. Two lens mounts were purchased in case it was decided that the twin beam output of the Wollaston prism needed to be focused on the detectors to prevent signal loss.

Optics were bought from both Coherent and Thorlabs. Since we were operating at such a precise frequency, 632.8 nm, it made the most sense to buy optics specifically tuned for HeNe⁹ lasers. This would give us the best performance for the price. However, Thorlabs has a line of broadband dielectric mirrors that provide more than 99% reflectivity at a 45° of both the S and the P¹⁰ polarizations. These mirrors feature a 15-5 scratch-dig¹¹ and are flat over the surface¹² of the optics to within $\frac{\lambda}{10}$. The Coherent beam splitters used were of the non-polarizing variety which were tuned for HeNe light at 632.8 nm, providing an almost exact 50/50 split of incident light at this wavelength, regardless of polarization.

⁸In the direction perpendicular to surface of the optic.

⁹Helium Neon.

¹⁰S polarization is when the E field is normal to the plane of incidence, while P polarization denotes that the E field is parallel to the plane of incidence.

¹¹Scratch-dig ratings are based on a subjective scale of how numerous and how large the scratches and pits on the surface of the optic. A rating of 40-20 is around the lower limit that the naked eye can detect. This rating was not overly important for our device, as any light reflected by any surface scratches will be directed out of the path of interferometer, meaning that it would just contribute to lost signal, and not lead to bad data.

¹²The flatness of the optic is usually measured in terms of some arbitrary wavelength usually around 633 nm. This specification was relatively important to our instrument, as an extremely flat optic would not contribute to distorting the shape, size, and coherence of the beam like a relatively curved optic would.

These beam splitters have scratch-dig of 10-5 and are flat to within $\frac{\lambda}{10}$. The Wollaston prism was also obtained from Coherent. The only choice in selecting this optic was size; we decided on the 12 mm aperture prism as the best combination of convenience and price. It has scratch-dig of 20-10 and is flat to $\frac{\lambda}{8}$ at 589 nm. Both waveplates were ordered from Thorlabs, who by far had the best price on these products. We decided to purchase the zero order waveplates, as these are not dependent on temperature, angle of incidence, and degree of collimation as multiple order waveplates are. Also, zero order waveplates are less sensitive to change in wavelength. Our waveplates, both the $\frac{\lambda}{2}$ plate and $\frac{\lambda}{4}$ plate, are specifically made for 633 nm light and possess a scratch-dig rating of 20-10 and are flat to $\frac{\lambda}{10}$. As the last optical component, we found it beneficial to use a filter centered at 632.8 nm to block out any unwanted signal, especially the $H\alpha$ light produced in the SSX discharge. This filter was obtained from Coherent and has a FWHM¹³ of 11 nm and has a minimum peak transmission of 80%.

We obtained most of the laser hardware from Newport, with the exception of the post and post base, which was bought from Thorlabs. The laser is mounted in a Newport mount, possessing adjusters for two axes, which is in turn installed on a post clamp, which attaches to the post. This structure gives us the most flexibility *and* security. The laser is a Uniphase 10 mw polarized HeNe laser with a polarization ratio of 500:1.

Detectors were purchased from Thorlabs and UDT Sensors. From Thorlabs, two high-speed amplified detectors, with a 50MHz bandwidth and a transimpedance gain of 1×10^4 V/A, were bought. However, these products are AC powered, and as this poses a problem in terms of possible AC line contamination during a plasma discharge, Photops detectors that are capable of operating under battery power were ordered from UDT Sensors. Originally, the Thorlabs detectors were going to be battery-powered, but it was discovered that they would run out a typical 9V battery in 10-15 minutes. The UDT detectors are also high-speed amplified detectors, but unlike the Thorlabs detectors, do not come packaged in a completed circuit layout. This enables one to determine the exact gain by final circuit design. The detectors have a Gain Bandwidth Product of ~ 20 MHz and Slew Rate of ~ 35 V/ μ s.

Two fused Silica vacuum viewports were bought from ISI for installation on SSX itself. These ports offer better than 90% transmission and a scratch-dig of at least 40-20.

¹³Full width at half maximum. At half transmission of the optic, this is the measure of the width of the filter, in terms of nm.

#	Component	Supplier	Product Number
2	2" HeNe Beam Splitters	Coherent	44-1634
3	2" Broadband Dielectric Mirrors	Thorlabs	BB2-R1
1	$\frac{\lambda}{2}$ Plate	Thorlabs	WPH0M-633
1	$\frac{\lambda}{4}$ Plate	Thorlabs	WPQ0M-633
1	Wollaston Prism	Coherent	43-8564
1	632.8 nm Bandpass Filter	Coherent	35-4126
1	10mW HeNe Laser	Newport	U-1335P
1	Tilt Laser Mount	Newport	ULM-TILT
1	Rod Clamp (for Laser Mount)	Newport	340-RC
1	8" Mounting Post	Thorlabs	P8A
1	Mounting Post Base	Thorlabs	PB1
5	2" Ultrastable Kinematic Mounts	Thorlabs	KS2
3	1" Ultrastable Kinematic Mounts	Thorlabs	KS1
2	Lense Mounts	Thorlabs	AC-1
1	Precision Rotation Stage	Thorlabs	PRM1
13	3" Posts	Thorlabs	TR3
13	3" Post Holders	Thorlabs	PH3-ST
13	Bases	Thorlabs	BA2
2	High-speed Amplified Photodetectors	Thorlabs	PDA155
2	Photops High-speed Photodetectors	UDT Sensors	UDT-455HS
2	Fused Silica Vacuum Viewports	ISI	9722005

Table 2: Component List

Appendix C: Gas Density Calibration

In order to check that the interferometer, detection instrumentation, and processing gear are interfaced properly, it is necessary to calibrate the device using a test medium of known index of refraction. Since the instrument is so sensitive and an ordinary glass window introduced into the scene beam introduces a shift of several hundred fringes, it is necessary to come up with a device with a much lower index of refraction than glass (around 1.52). It was decided to fabricate a chamber of known length (15cm) with glass windows on each side and two swagelock fittings installed. This allows one to evacuate the chamber to a known pressure using one of the swagelock fittings. By releasing the valve on the other fitting, one can produce a relatively quick pressure change of a known value inside the chamber. Since the index of refraction of air changes with its density in a linear manner, one can easily predict the amount of phase shift this sudden pressure drop brings about.

$$\begin{aligned}\Delta N &= \frac{l}{\lambda_1} - \frac{l}{\lambda_2} \\ &= l\Delta\left(\frac{1}{\lambda}\right) \\ &= l(-\lambda^2\Delta\lambda)\end{aligned}\tag{47}$$

Where l is the length of the chamber. In order to proceed from equation 47, one must calculate the value of $\Delta\lambda$. It is helpful to know the relation seen in equation 48.

$$\begin{aligned}\lambda &= \frac{v}{\nu} = \frac{c}{\nu n} \\ \Delta\lambda &= \frac{\Delta v}{\nu} \\ &= \frac{c}{\nu} \left(\frac{1}{n_1} - \frac{1}{n_2} \right)\end{aligned}\tag{48}$$

From this point, one can quickly solve for the amount of fringe shift (ΔN) in terms of cavity length (l), wavelength (λ), and the indices of refraction (n_1 and n_2).

$$\Delta N = -\frac{cl}{\lambda^2\nu} \left(\frac{1}{n_1} - \frac{1}{n_2} \right) = -\frac{l}{\lambda} \left(\frac{1}{n_1} - \frac{1}{n_2} \right)\tag{50}$$

The index of refraction for air is 1.000292. At a pressure of ~ 660 mmHg, the index of refraction is 1.000253, calculated by the fact that the index of refraction scales linearly with the density of air. Using this figure and length of the chamber as 15cm, one would expect to measure approximately 9 fringes going by when letting this partial vacuum equilibrate with normal atmospheric pressures. When this was measurement was performed, we measured about $5\frac{1}{2}$ fringes (see fig. 26). Using the experimental data and back into equation 49, this measured fringe shift predicts an pressure of about ~ 700 mmHg. Since the measurement of the pressure inside the chamber was done with a simple handpump/gauge, this is a relatively small error.

Another measurement made with this same apparatus was the pumping of helium into the calibration chamber. This was performed by turning the calibration chamber so that both

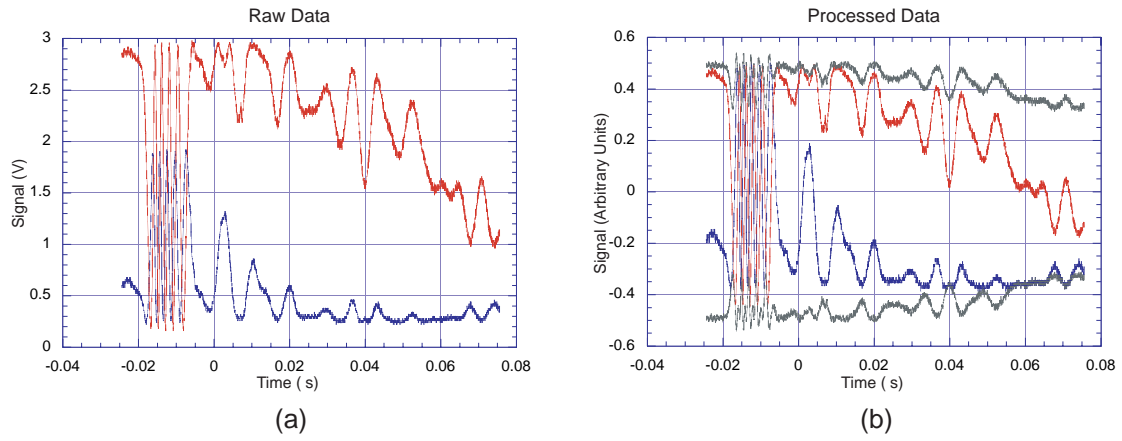


Figure 25: Output of the detectors from an evacuated to normal atmospheric pressure run. (a) Raw data from the two detectors. (b) Processed data from the two detectors. Both signals have been normalized and centered about the origin. The gray lines signify the fringe envelope amplitude.

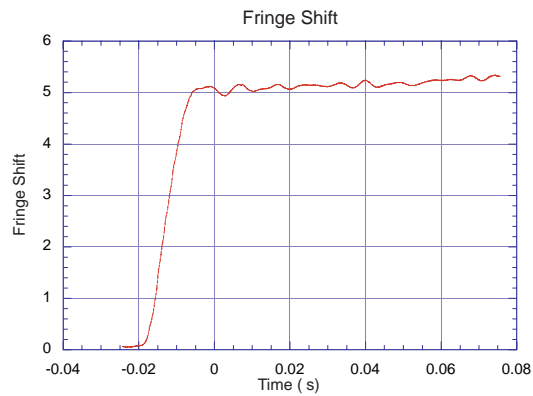


Figure 26: The fringe shift associated with the raw data from figure 25.

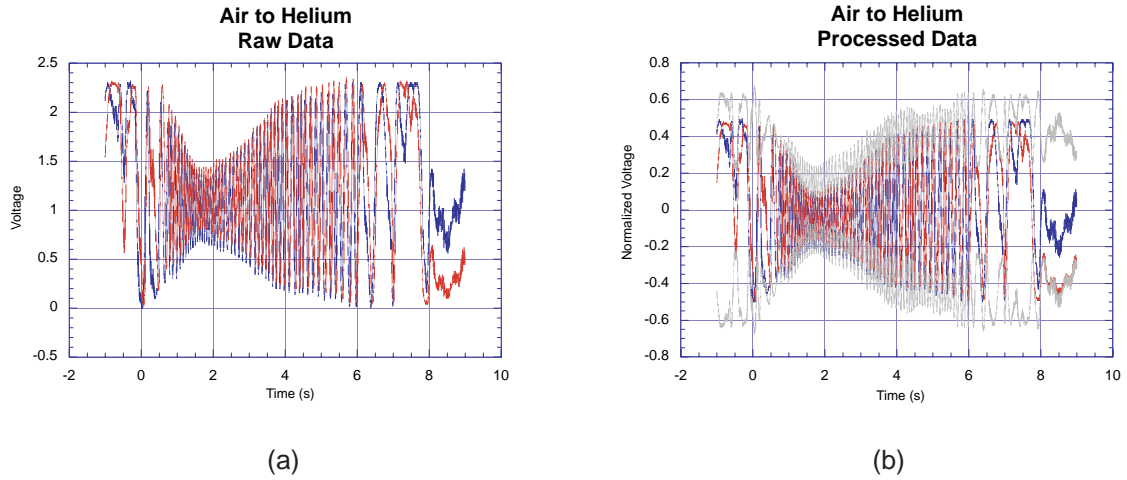


Figure 27: Output of the detectors in a air to helium calibration run (a) Raw data from the two detectors. (b) Processed data from the two detectors. Both signals have been normalized and centered about the origin. The gray lines signify the fringe envelope amplitude.

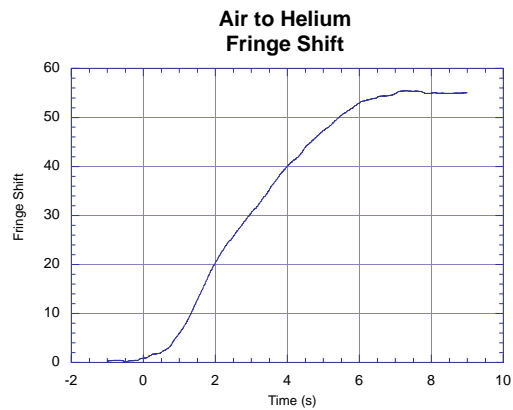


Figure 28: The fringe shift associated with the raw data from figure 27.

swagelock fittings were on the bottom. When the helium was turned on, it pushed the air in the chamber out of the other orifice, since helium is lighter than air. In other words, the air “fell” out of the chamber. Since Helium’s index of refraction is only 1.000036 compared to air’s 1.0002926, we expected to see a fringe shift of 60.8 while doing this. Experimental results showed a fringe shift of ~ 55 , as show in figures 27 and 28. This is very close to the desired result when one considers that when the measurement is concluded, it is hard to verify if all of the air in the chamber has really been displaced by the helium.

Appendix D: Analysis Routines

These analysis programs were run in Matlab 5.2 on an Apple Power Mac G4 450 MHz.

D.1 Interferometer Routine

```
% Refer to dataanalysis.pdf for assigning of variable names
clear all;
filename = input('File Name? ', 's');
filt=input('Reduction factor? ');
ki=[1.852 1.641]; % k1&k2 Max amplitude of signals (Range assuming min=0)

% ---- FILE HANDLING ---- %

fid=fopen(filename); %fid = file identifier #
file_header_string=fgetl(fid); %Read header & make a matrix of it
header={};
k=1; name='';
for i=1:size(file_header_string,2)
    ch=file_header_string(i);
    if (ch~=' ')
        name=[name ch];
    else
        header{k}=name;
        name='';
        k=k+1;
    end
end

[filematrix,count]=fscanf(fid,'%e',[size(header,2),5000000]);
%reads the rest of the data %(excluding headers)
filematrix=filematrix';
fclose(fid); %We're done with it now.

for i=1:size(header,2) %assigns names to data columns
    switch header{i}
        case 't-secs', time=filematrix(:,i)';
        case 'Int 1', S1=filematrix(:,i)';
        case 'Int 2', S2=filematrix(:,i)';
    end
end
```

```

% ---- FILTERING AND AVERAGING ---- %

if (filt ~= 0)
    ed=reshape(S1,filt,length(S1)/filt);
    ed2=reshape(S2,filt,length(S2)/filt);
    ed3=reshape(time,filt,length(time)/filt);
    clear S1 S2 time;
    for i=1:length(ed)
        S1(i)=sum(ed(:,i))/filt;
        S2(i)=sum(ed2(:,i))/filt;
        time(i)=sum(ed3(:,i))/filt;
    end
end

% ---- ANALYSIS ---- %

baseline=[sum(S1(1,1:10))/10 sum(S2(1,1:10))/10]; % V1 and V2

dv1=S1-baseline(1); % DV1 and DV2
dv2=S2-baseline(2);
dphi=acos(1-.5.*((dv1/ki(1)).^2+(dv2/ki(2)).^2))*180/pi; %Dphi

Density=(dphi * 8*pi*3e8*8.854e-12 *9.109e-31)/((1.602e-19)^2*632.8e-9);

figure
plot(time,Density);

```

D.2 Triple Probe Routine

```

%clear all;
filename='r22';
Vd3=36.5; %Volts

area=3.6/1000^2; %Area of probe tip in cubic meters.

e=1.6E-19; %Electron charge (C)
mi=938.27E6; %Proton mass (eV/c^2)
c=3.0E8; %Speed of light (m/s)

fid=fopen(filename); %fid = file identifier #

```

```

file_header_string=fgetl(fid); %Read header & make a matrix of it

%Count up the number of columns, place the header string in a struct array
header={};
k=1; name='';
for i=1:size(file_header_string,2)
    ch=file_header_string(i);
    if (ch~=' ')
        name=[name ch];
    else
        header{k}=name;
        name='';
        k=k+1;
    end
end
clear k ch file_header_string name;

[filematrix,count]=fscanf(fid,'%e',[size(header,2),5000000]);
%reads the rest of the data (excluding headers)
filematrix=filematrix';
fclose(fid); %We're done with it now.

for i=1:size(header,2)
    switch header{i}
        case 't-secs', time=filematrix(:,i)';
        case 'Vd2', Vd2=filematrix(:,i)'*100;
            %Isolation transformer set to 100 times.
        case 'I', I1=filematrix(:,i)'.*(10); %Current transformer is 10 times.
    end
end

%Apply 1/10 FIR filter
Vd2=firfilter(Vd2);
I1=firfilter(I1);

%Sparse 10 times:
Vd2=Vd2([1:10:end]);
I1=I1([1:10:end]);
time=time([1:10:end]);

%tempseries=temperature(Vd2,Vd3);

%Don't let current go negative:
I1(I1<0)=.001;

```

```

%actual calculation
consts=exp(1/2)/(area*e);

%approximation
tempseries1=Vd2*1.44;
soundspeed1=sqrt(tempseries1/(mi/c^2));
densityseries1= I1 .* exp(1/2)./(area.*e.*soundspeed1) / 100^3;

figure
hold on;
%subplot(2,1,1);
%plot(time,tempseries,time,Vd2*1.44);
line([4e-5 4e-5],[-10 30]);
plot(time,tempseries1,'g');
title(['Temperature (File: ' filename ', Voltage: ' num2str(Vd3) 'V)']);
xlabel('Time (s)');
ylabel('\itT_{e} (eV)');

figure
hold on;
%subplot(2,1,2);
%plot(time,densityseries,time,densityseries1);
line([4e-5 4e-5],[0 10e14]);
plot(time,densityseries1,'g');
title(['Density (File: ' filename ', Voltage: ' num2str(Vd3) 'V)']);%
xlabel('Time (s)');
ylabel('\itn (cm^{-3})');

ginput

```

Appendix E: Acknowledgements

The author would like to thank his thesis advisor, Michael Brown, and coworkers Dave Schlossberg, Slava Lukin, and Andrew Fefferman for the tremendous help in completing the work required for this thesis. Steve Palmer was invaluable for helping to construct the interferometer mount. Thanks also to Dave Auerbach, Dave Radcliff, Frank Moscatelli, and to the Swarthmore College Physics and Astronomy Department.

References

- Bellan, P. M. (2000). *Spheromaks: A Practical Application of Magnetohydrodynamic Dynamics and Plasma Self-Organization*. Imperial College Press, London.
- Brown, M. R. (1996). Spheromak experiment using separate guns for formation and sustainment. *Fusion Technology*, 30(3):300.
- Brown, M. R. (1997). Experimental evidence of rapid relaxation to large-scale structures in turbulent fluids: selective decay and maximal entropy. *Journal of Plasma Physics*, 57:203.
- Brown, M. R. (1999). Experimental studies of magnetic reconnection. *Physics of Plasmas*, 6(5):1717.
- Buchenauer, C. J. and Jacobson, A. R. (1977). Quadrature interferometer for plasma density measurement. *Review of Scientific Instrumentation*, 48(7):769.
- Chen, F. F. (1984). *Introduction to Plasma Physics and Controlled Fusion*. Plenum Press, New York.
- Cohen, S. A. (1995). Laboratory in plasma physics. Unpublished lab manual.
- Geddes, C. G. R. (1997). Equilibrium studies on ssx. Undergraduate thesis, Swarthmore College.
- Geddes, C. G. R., Kornack, T. W., and Brown, M. R. (1998). Scaling studies of spheromak formation and equilibrium. *Physics of Plasmas*, 5(4):1027.
- Hariharan, P. (1992). *Basics of Interferometry*. Academic Press, Inc., San Diego.
- Huddleston, R. and Leonard, S. L. (1965). *Plasma Diagnostic Techniques*. Academic Press, New York.
- Hutchinson, I. H. (1987). *Principles of Plasma Diagnostics*. Cambridge University Press, Cambridge.
- Jacobson, A. R. (1982). Technique for direct phase demodulation in heterodyne interferometry. *Review of Scientific Instrumentation*, 53(6):918.
- Jenkins, F. A. and White, H. E. (1976). *Fundamentals of Optics, 4th ed.* McGraw-Hill, New York.
- Ji, H., Toyama, H., Yamagishi, K., Shinohara, S., Fujisawa, A., and Miyamoto, K. (1991). Probe measurements on the repute-1 reversed field pinch. *Review of Scientific Instrumentation*, 62(10):2326.
- Kornack, T. W. (1998). Magnetic reconnection studies on ssx. Undergraduate thesis, Swarthmore College.

- Kornack, T. W., Geddes, C. G. R., and Brown, M. R. (1998). Experimental observation of correlated magnetic reconnection and alfvénic ion jets. *Physical Review E*, 58(1):36.
- Kristal, R. and Peterson, R. W. (1976). Bragg cell heterodyne interferometry of fast plasma events. *Review of Scientific Instrumentation*, 47(11):1357.
- Lowenthal, D. D. and Hoffman, A. L. (1979). Quasi-quadrature interferometer for plasma density radial profile measurements. *Review of Scientific Instrumentation*, 50(7):835.
- Lukin, V. (2000). Modeling ssx spheromak plasmas: internal physics from external measurements. Undergraduate thesis, Swarthmore College.
- Owens, K. (1980). Lecture 4: Langmuir probes. Unpublished lecture notes.
- Park, H. K. (1989). A new asymmetric Abel-inversion method for plasma interferometry in tokamaks. *Plasma Physics and Controlled Fusion*, 31(13):2035.
- Schlossberg, D. (2001). Energetic particle studies from reconnection experiments on ssx. Undergraduate thesis, Swarthmore College.
- Sheridan, T. E. (2000). How big is a small langmuir probe? *Physics of Plasmas*, 7(7):3084.
- Steel, W. H. (1983). *Interferometry, 2nd ed.* Cambridge University Press, Cambridge.
- Wong, A. Y. (1977). *Introduction to Experiment Plasma Physics, Vol. 1.* Academic Publishing Service, Los Angeles.